MOLECULAR BIOLOGY

ACSS2 coupled with KAT7 regulates histone β-hydroxybutyrylation to enhance transcription

Siyu Wang[1]†, Ziping Niu[1]†, Yingao Zhang[1], Ruilong Liu[2], Rui Zhu[1], Yuxuan Sun[1], Yanpu Han[1], Aiyuan Wang[1], Jianji Zhang[1], Hui Zhang[1], Yong Zang[1], Yingming Zhao[2], Guijin Zhai[1]*, Kai Zhang[1,3]*

Histone lysine β-hydroxybutyrylation (Kbhb) is an epigenetic mark linking ketone metabolism to transcription. However, the molecular mechanism by which β-hydroxybutyrate is converted to β-hydroxybutyryl–coenzyme A (BHB-CoA), the cofactor for Kbhb, remains unknown. Here, we report that acetyl-CoA synthetase short-chain family member 2 (ACSS2) coupled with lysine acetyltransferase 7 (KAT7) modulates β-hydroxybutyrylation on lysine 9 of histone H3 (H3K9bhb) to promote transcription. We show that KAT7 serves as a β-hydroxybutyryltransferase and preferably catalyzes histone Kbhb, especially H3K9bhb, in 1171 identified Kbhb substrates. ACSS2 is a BHB-CoA synthetase. This enzyme can sense cellular β-hydroxybutyrate and translocate into the nucleus, where it binds to and colocalizes with KAT7 at specific locus of chromatin. The ACSS2-generated BHB-CoA can fuel KAT7 for histone H3K9bhb. We demonstrate that the β-hydroxybutyrate drives the ACSS2-KAT7-H3K9bhb axis to promote epigenetic regulation and tumor cell growth. Our study not only identifies the founding member of BHB-CoA ligase but also reveals the mechanism underlying KAT7-catalyzed histone Kbhb using ACSS2-generated BHB-CoA.

INTRODUCTION

The metabolic rewiring and extended fasting lead to a substantial rise in hepatic ketogenesis, the resulting elevation of ketone bodies in the circulation (*1*, *2*). Ketone bodies serve as fatty acid–derived carbon fuels that, in turn, provide an energy source to other tissues such as the brain and heart for the generation of acetyl–coenzyme A (CoA) (*3*–*5*). Among the ketones, β-hydroxybutyrate (BHB) has been implicated in the regulation of tumorigenesis by binding to surface receptor hydroxycarboxylic acid receptor 2 and thereby altering gene expression and cell proliferation (*6*), suggesting that BHB may play a noncanonical role in multiple biological processes (*7*, *8*).

BHB has recently been recognized as a donor for lysine β-hydroxybutyrylation (Kbhb), a type of protein posttranslational modification (PTM) (*9*). The Kbhb has been detected in diverse eukaryotes ranging from yeast to human. Forty-four histone Kbhb marks were identified previously (*10*, *11*). Emerging evidence suggests that histone Kbhb marks couple closely with cellular metabolism that, in turn, regulates gene transcription and functional outputs (*12*–*15*). For example, Huang group (*16*) shows that ketogenesis-generated BHB stimulates β-hydroxybutyrylation on lysine 9 of histone H3 (H3K9bhb) and promotes transcription along with $CD8^+$ T cell memory development. Besides, Terranova *et al.* (*17*) demonstrate that fasting induces BHB production in small intestine cells, which preferably facilitates the enrichment of histone H3K9bhb, but not histone H4K12bhb, at metabolic genes and the expression of these genes. Moreover, the metastasis associated 1 family member 2-RNA-DNA hybrid loop-3-hydroxybutyrate dehydrogenase 1-histone (MTA2–R loop–BDH1–histone) H3K9bhb axis was suggested to mediate the expression of its target genes via regulation of BHB, and its potentiation of hepatocellular carcinoma cell propagation is reported (*18*). These studies suggest a model that BHB fuels histone Kbhb that, in turn, regulates gene expression. BHB-CoA can serve as a cofactor for histone Kbhb (*9*). Nevertheless, it remains unknown how cellular BHB is converted to BHB-CoA for Kbhb, representing an important gap in this PTM and epigenetic pathway.

Here, we report the identification of acetyl-CoA synthetase short-chain family member 2 (ACSS2) as the founding member of BHB-CoA synthetase. We showed that lysine acetyltransferase 7 (KAT7) can serve as a histone β-hydroxybutyryltransferase that preferably catalyzes H3K9bhb using ACSS2-generated BHB-CoA. Moreover, we demonstrate that ACSS2 can sense intracellular BHB and translocate into the nucleus, where it binds to and colocalizes with KAT7 at a specific locus of chromatin. Cleavage under targets and tagmentation (CUT&Tag) and RNA sequencing (RNA-seq) analyses reveal that ACSS2-KAT7 interaction drives the expression of several target genes that are associated with cancer cell growth through elevating histone H3K9bhb. Together, our findings show a mechanism that ACSS2 couples with KAT7 to promote histone H3K9bhb and gene transcription, bridging an important gap in the histone Kbhb pathway.

RESULTS

KAT7 serves as a histone β-hydroxybutyryltransferase

Emerging evidence indicates that histone Kbhb induced by BHB plays a key role in the regulation of ketone metabolism (*19*). However, the molecular mechanism by which BHB is converted to Kbhb in specific chromatin loci remains unclear. So, we first aim to explore the writer that catalyzes the addition of this modification. There are three major families of characterized histone acetyltransferase [HAT; p300/CREB-binding protein, Gcn5-related N-acetyltransferase (GNAT), and MYST] (*20*), displaying an expanded acyltransferase activity

[1]Key Laboratory of Breast Cancer Prevention and Therapy (Ministry of Education), Key Laboratory of Immune Microenvironment and Disease (Ministry of Education), The Province and Ministry Co-sponsored Collaborative Innovation Center for Medical Epigenetics, School of Basic Medical Sciences, Tianjin Medical University Cancer Institute and Hospital, Tianjin Medical University, Tianjin 300070, China. [2]Ben May Department for Cancer Research, The University of Chicago, Chicago, IL 60637, USA. [3]Tianjin Key Laboratory of Digestive Diseases, Department of Gastroenterology and Hepatology, Medical University General Hospital, Tianjin Medical University, Tianjin 300070, China.
*Corresponding author. Email: zhaiguijin@tmu.edu.cn (G.Z.); kzhang@tmu.edu.cn (K.Z.)
†These authors contributed equally to this work.

(*21*, *22*). Given the facts that p300 is the most promiscuous acyltransferase and shows catalytic activity for limited histone Kbhb sites (*23*) while GNAT members have a more restricted activity for acylation (*24*, *25*), we therefore focus on the MYST family.

To test whether a member of the MYST family acts as a β-hydroxybutyryltransferase, we treated cells with the specific inhibitors of KAT5, KAT6A/KAT6B, KAT7, and KAT8, respectively, and determined the Kbhb levels using a pan-Kbhb antibody. As shown in Fig. 1A, the inhibition of KAT7 leads to the most obvious decrease in histone Kbhb level among them. Hence, we established KAT7 knockdown (KD) in multiple cell lines [e.g., HeLa, human embryonic kidney (HEK) 293 T cells (HEK-293T), and Hepatoblastoma cell line G2 (HepG2)] with specific short hairpin RNA (shRNA) and found that the Kbhb level was significantly reduced owing to KAT7 KD (Fig. 1B and fig. S1, A and B), in line with the observations from KAT7-deficient cells (Fig. 1C and figs. S1, C and D, and S2, A to C). Conversely, the overexpression of KAT7 promotes histone Kbhb (Fig. 1D and fig. S1, E and F). A gradual increase in BHB markedly elevates Kbhb instead of lysine acetylation (Kac) in wild-type (WT)–KAT7 cells, while KAT7 depletion failed to enhance the Kbhb level, suggesting that BHB fuels KAT7 primarily for Kbhb, but not Kac (Fig. 1C and fig. S2, B and C). Besides, immunofluorescence (IF) staining analysis showed the colocalization of Kbhb and KAT7 (Fig. 1E and fig. S2, E and F). These findings demonstrate that KAT7 can catalyze the generation of histone Kbhb in cells.

To gain insights into the catalytic activity of KAT7 for Kbhb, we performed an in vitro pan-Kbhb assay using the recombinant catalytic domain of KAT7 and showed that the histone Kbhb levels were markedly elevated with the prolongation of reaction time, implying a direct catalysis of KAT7 for Kbhb (Fig. 1F). Moreover, structural analysis suggested that KAT7 binds to BHB-CoA through several key residues including G485 and E508 (fig. S2D). Accordingly, mutation of these residues did cause the decrease in Kbhb, whereas the ectopic expression of WT-KAT7, but not its mutants, allowed restoring this reduction (fig. S1, G and H). Together, the results further verified that KAT7 is directly responsible for Kbhb, relying on its key residues.

Identification of the endogenous Kbhb substrates targeted by KAT7

Next, we identified the landscape of endogenous Kbhb substrates targeted by KAT7. Western blotting (WB) analysis suggested that KAT7 may have activity in the global Kbhb (fig. S2, A to C). We therefore identified the potential substrates of KAT7 by a stable isotope labeling by amino acids in cell culture (SILAC)–based quantitative proteomics approach. The proteins were extracted from KAT7-WT and KAT7–knockout (KO) cells, respectively, and mixed equally, followed by tryptic digestion, enrichment of Kbhb peptides with pan-Kbhb antibody, and liquid chromatography–tandem mass spectrometry (LC-MS/MS) analysis (fig. S3A). Consequently, 1171 Kbhb sites were identified in 582 proteins, 41% of which bear multiple sites (Fig. 2A, fig. S3, B to D, and table S1). The motif analysis of the identified Kbhb sites using iceLogo revealed that positively charged amino acids had more notable preference for most positions (−7, −6, −5, −4, −3, −2, 4, 5, 6, and 7), while hydrophobic amino acids such as Leu and Phe were overrepresented at the +1 position (fig. S3E). We defined the KAT7-mediated sites with a cutoff of fold change (1.5-fold) via normalizing the Kbhb ratio of heavy isotope/light isotope (H/L) with the counterpart protein ratio (H/L), followed by Gene Ontology (GO) analysis of KAT7-regulated Kbhb sites. Notably, they are mostly involved in epigenetic regulatory pathways including chromatin remodeling, nucleosome assembly, and nucleosome organization, suggesting that KAT7-mediated substrates of Kbhb plays a crucial part in gene transcription (Fig. 2B).

Having established that KAT7 catalyzing substrates of Kbhb involved in epigenetic regulation and given that the function of KAT7 in the regulation of transcription and DNA replications (*26*–*28*), we moved to focus on KAT7-regulated Kbhb sites on histones. Accordingly, we identified 73 histone Kbhb marks, 21 of which were regulated by KAT7 (Fig. 2, C and D, and table S2). Notably, H3K9bhb displayed the most significant decrease in these KAT7-mediated Kbhb sites, which was further confirmed by LC-MS/MS analysis (fig. S4A). Overexpression of KAT7 boosted H3K9bhb; in contrast, KAT7 depletion significantly abolished it (Fig. 2, E to G, and fig. S4, B to G). Together with IF assay (Fig. 2, H and I), these results indicate that KAT7 can regulate histone Kbhb, preferring H3K9bhb. Of note, the H3K9bhb level was not significantly reduced in the KAT5-deficient cells, suggesting the specific regulation of H3K9bhb by KAT7 in eukaryotes (fig. S4H).

ACSS2 senses BHB to translocate into the nucleus and interacts with KAT7

Currently, the molecular mechanism by which BHB is converted to BHB-CoA, the cofactor for histone Kbhb, remains unknown, representing an important gap in this PTM and epigenetic pathway. To understand it, we investigated the factors that assist KAT7 in regulating H3K9bhb. We assumed reasonably that the candidate facilitators may have two general features: (i) they are induced by BHB and (ii) interact with KAT7. So, we designed two sets of quantitative proteomics experiments, wherein cells were cultured in the presence or absence of BHB, as well as cells transfected with Flag-KAT7 or Flag-vector, followed by protein isolation and quantification. This enabled us to mine candidate proteins that have high enrichment ratios and statistical significance in both +BHB/–BHB and Flag-KAT7/Flag-vector experiments (Fig. 3A and figs. S5, A and B, and S6A). As a result, the two sets of experiments revealed numerous targets that were involved in a range of pathways such as nucleocytoplasmic transport (figs. S5, C and D, and S6, B and C). Notably, in the proteins identified in both sets (Fig. 3B and table S3), ACSS2 attracted our interest due to its activity as a chromatin coactivator for histone acetylation (*29*–*31*).

To examine whether BHB is linked to ACSS2, we first determined the ACSS2 expression level in BHB-treated HeLa cells and observed a rise in the protein abundance with BHB in a dose-dependent manner (Fig. 3F). Murthy *et al.* (*32*) had observed an increase in ACSS2 levels in acetate-treated cancer cells. Moreover, the cell fraction assay revealed that BHB induced an obvious ACSS2 accumulation in the nucleus instead of the cytoplasm (Fig. 3G). Similarly, IF analysis also indicated the nuclear translocation of ACSS2 in the presence of BHB (Fig. 3E and fig. S7A). Given that epidermal growth factor–dependent phosphorylation of ACSS2 facilitates its translocation into the nucleus (*33*), we hypothesized that BHB treatment might promote ACSS2 phosphorylation, thereby leading it into the nucleus. To test this hypothesis, we conducted immunoprecipitation (IP)–MS/MS analysis on cells ectopically expressing ACSS2 in the presence of BHB. We identified S267 phosphorylation (pS267) of ACSS2, one mark that has been unveiled to promote importin α_5-dependent translocation of ACSS2 (*33*) in cells treated with BHB

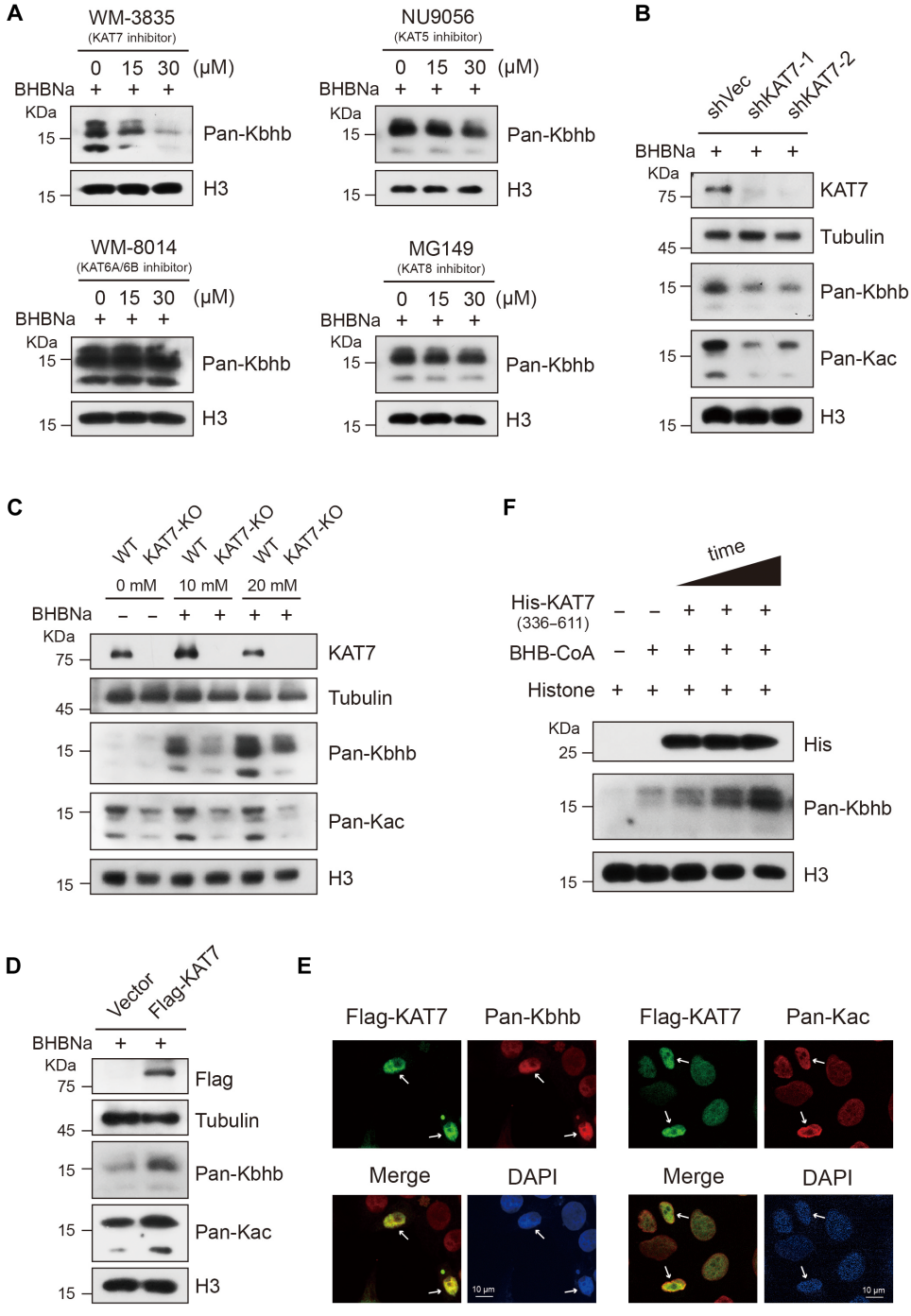

Fig. 1. KAT7 regulates histone β-hydroxybutyrylation in eukaryocytes. (**A**) In vivo screening of β-hydroxybutyryltransferase activity for MYST family acetyltransferases in HeLa cells by their corresponding inhibitors. WM-3835: a specific inhibitor of KAT7, NU9056: a specific inhibitor of KAT5, WM-8014: an inhibitor of KAT6A/KAT6B, and MG149: an inhibitor of KAT8. (**B**) Western blot (WB) analysis of the level of Kbhb on histones in KAT7-KD HeLa cells. shVec, empty vector as control group; shKAT7-1/2, vector containing two sequences (short hairpin RNA-1/2) for depletion of KAT7. The cells were pretreated with 10 mM BHB sodium (BHBNa). (**C**) Determination of histone β-hydroxybutyrylation in KAT7-KO HeLa cells with the gradient BHBNa treatment. BHBNa treatment dose-dependently elevated the Kbhb levels in WT cells, but this increase was blunted in KAT7-depleted cells. (**D**) Measurement of the level of Kbhb on histones by WB analysis in HeLa cells overexpressing KAT7. (**E**) IF staining showing the colocalization between KAT7 and Kbhb and an increased Kbhb level resulting from KAT7 overexpression in HeLa cells. Kac was used as a control. The HeLa cells were transfected with Flag-tagged KAT7, followed by treatment with antibodies against Flag (green) or pan-Kbhb antibody (red). Scale bars, 10 μm. (**F**) Immunoblot analysis of Kbhb by in vitro assay. The catalytic domain of KAT7 was recombinantly expressed and incubated with core histones in the presence of BHB-CoA. The histone Kbhb was detected at different incubation time points (10, 20, and 30 min).

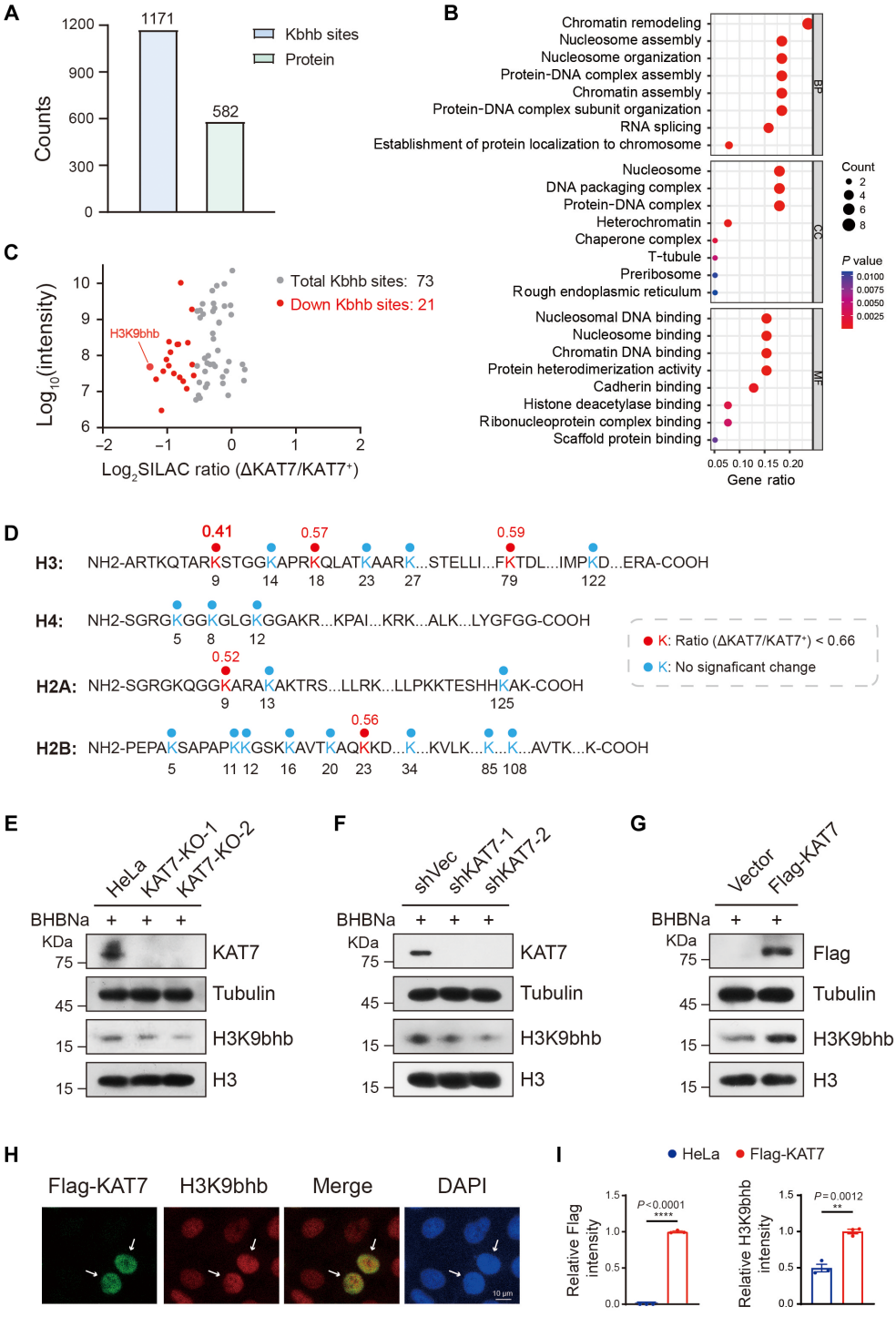

Fig. 2. Identification of endogenous Kbhb substrates of KAT7. (**A**) Bar graph suggesting the number of Kbhb sites and Kbhb-modified proteins identified in HeLa cells. (**B**) GO analysis for KAT7-regulated Kbhb sites. The *P* value cutoff = 0.05 and *q* value cutoff = 0.1 were selected as the cutoff criteria. Benjamini and Hochberg correction was used to adjust *P* values. BP, biological process; CC, cellular component; MF, molecular function. (**C**) Scatter plot showing the ratio of Kbhb peptides of histones in KAT7-KO HeLa cells versus WT HeLa cells. Twenty-one histone Kbhb sites were down-regulated by KAT7, and H3K9bhb showed the most significant decrease among them. (**D**) Illustration of histone Kbhb sites regulated by KAT7. (**E** and **F**) WB assays of H3K9bhb on histones in KAT7-KO (E) or KAT7-KD (F) HeLa cells. (**G**) Immunoblot analysis of H3K9bhb in KAT7-overexpressed HeLa cells. "BHB +" means HeLa cells with the treatment of 10 mM BHBNa. (**H**) IF staining showing the colocalization of H3K9bhb and KAT7 in cells. The HeLa cells were transfected with Flag-tagged KAT7 in the presence of 10 mM BHBNa and then treated with antibodies against Flag (green) or H3K9bhb antibody (red). Scale bar, 10 μm. (**I**) The relative H3K9bhb intensity of IF in HeLa cells ectopically expressing Flag-KAT7 is shown [related to (H)]. The blue point represents HeLa cells without ectopic expression of Flag-KAT7, while the red point represents HeLa cells with ectopic expression of Flag-KAT7. The bar chart showing the mean ± SEM of the three independent experiments. $^{**}P < 0.01$ and $^{****}P < 0.0001$.

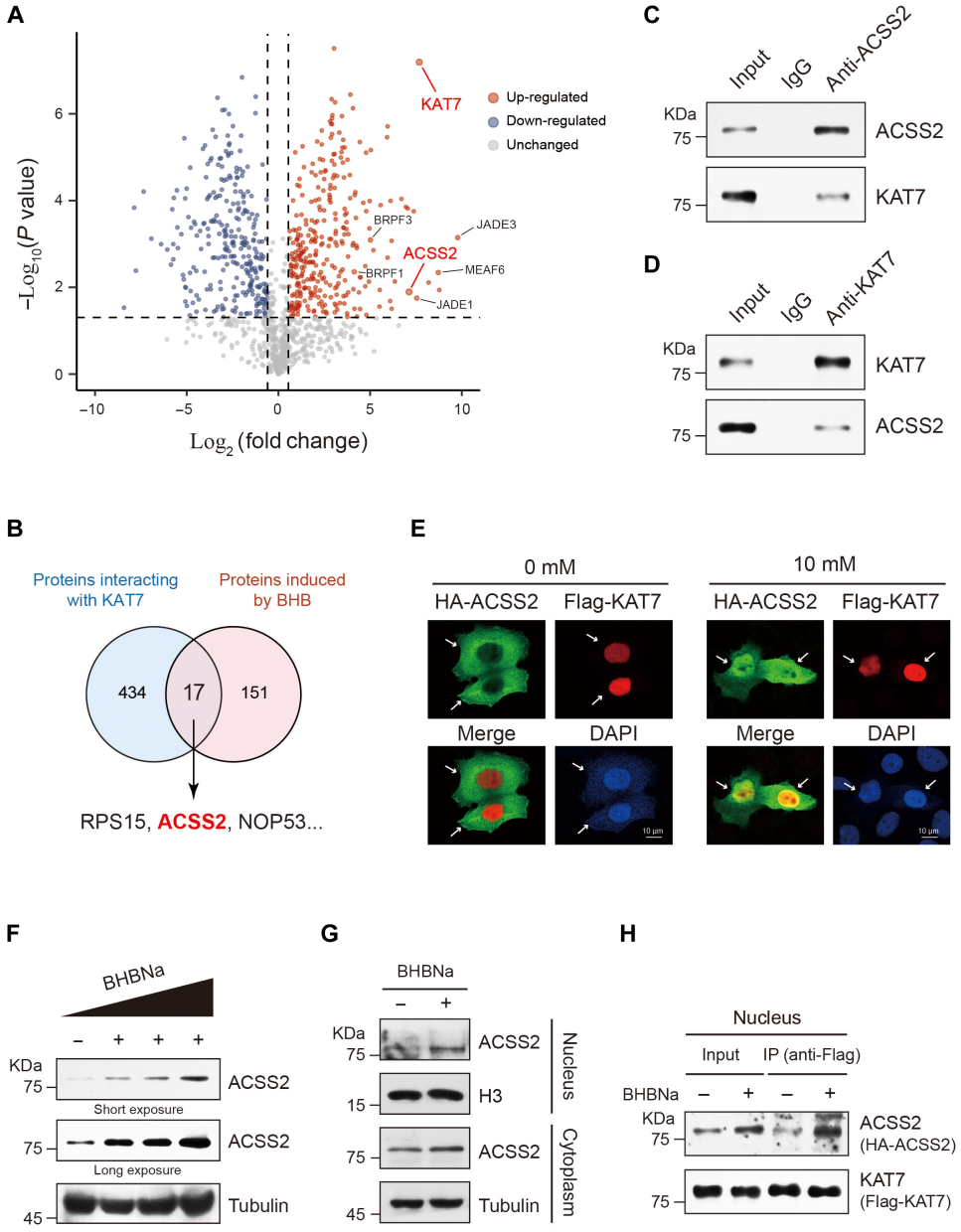

Fig. 3. BHB induces the translocation of ACSS2 into the nucleus where it interacts with KAT7. (**A**) Volcano plot depicting proteins identified by KAT7 immunoprecipitation (IP)/MS in BHB-stimulated HeLa cells [1.5–fold change (FC) cutoff, $P < 0.05$, $n = 3$ in each group, from independent biological replicates]. BRPF1/3, bromodomain and PHD finger-containing protein 1/3; JADE1/3, JADE family PHD finger protein 1/3; MEAF6, MYST/Esa1-associated factor 6. (**B**) Venn diagram showing candidate proteins satisfied with the criteria throughout combinatorial proteomics analysis. (**C** and **D**) Co-IP and reciprocal IP assays for verifying the interaction between endogenous KAT7 and ACSS2. (**E**) IF staining showing that ACSS2 is transported from the cytoplasm to the nucleus upon BHBNa stimulation, followed by colocalization with KAT7 in the nucleus. HA, hemagglutinin. (**F**) Immunoblot of ACSS2 in HeLa cells upon the gradient BHBNa treatment in short (top) or long (bottom) exposure time. The concentration gradient was as follows: 0, 5, 10, and 20 mM. (**G**) Immunoblot detection displaying the distribution of ACSS2 in the cytosolic (bottom) and nuclear (top) with or without BHBNa stimulation. (**H**) Immunoblot analysis showing ACSS2 level enriched by relatively equal KAT7 in the nucleus with or without BHB addition.

(fig. S7B). These results suggest that BHB not only facilitates ACSS2 expression but also enhances its nuclear accumulation through promoting the pS267 of ACSS2.

We further showed the interaction between exogenous or endogenous ACSS2 and KAT7 by performing Co-IP and reciprocal IP detection (Fig. 3, C and D, and fig. S8A). This interaction was further confirmed by an in vitro pull-down assay (fig. S8B). IF assay showed that ACSS2 and KAT7 were colocalized to cellular nuclei to a greater degree with BHB treatment (Fig. 3E and fig. S7A). Hence, we moved to explore whether BHB treatment contributes to the interaction between ACSS2 and KAT7 in different cell fractions (fig. S8, C to F). The results revealed that this interaction occurs regardless of the presence of BHB, whereas BHB indeed enhanced the interaction in the nucleus rather than in the cytoplasm (Fig. 3H and fig. S7C).

Collectively, these data indicate that ACSS2 can sense cellular BHB and translocate into the nucleus where it binds to KAT7 (fig. S7D).

ACSS2 fuels histone Kbhb through the generation of BHB-CoA

Next, we inferred that ACSS2 is a BHB-CoA synthetase that converts BHB to BHB-CoA for histone Kbhb, considering that it enables the supply of acetyl-CoA for protein acetylation by capturing acetate (*34*). To verify this, we first examined the Kbhb levels in multiple cells (including HeLa, HEK-293T, and HepG2 cells) with ectopic expression of ACSS2 in the presence of BHB and found an increase in a global Kbhb level and H3K9bhb, but not histone H3 lysine 9 acetylation (H3K9ac; Fig. 4A and fig. S9, A and B). In contrast, limiting ACSS2 by either genetic depletion or leveraging its specific inhibitor (ACSS2 inhibitor had no obvious interference on the expression of ACSS2) led to a pronounced decrease in the Kbhb level (Fig. 4, B to E, and fig. S9, C to F). We treated cells with ACSS2 inhibitors alone and performed WB analysis. Consequently, the results demonstrated that ACSS2 inhibition led to a significant reduction in both pan-Kac and H3K9ac (fig. S9, G and H). Of note, cells incubated with ACSS2 inhibitor and BHB showed decreased H3K9bhb rather than H3K9ac (Fig. 4, D and E), indicating that high concentrations of BHB could compete with acetate and therefore mainly fuel ACSS2 for BHB-CoA conversion and Kbhb catalysis. Moreover, IF assay confirmed the colocalization between ACSS2 and H3K9bhb and the promotion of H3K9bhb, but not H3K9ac, by ACSS2 (Fig. 4F and fig. S10, A to C). Of note, coexpression of ACSS2 and KAT7 greatly enhanced H3K9bhb rather than H3K9ac in the presence of BHB (fig. S10D). These results suggest that ACSS2 is able to preferably regulate histone H3K9bhb, but not H3K9ac, coordinating with KAT7 in the presence of BHB.

To confirm that ACSS2 contributes to the generation of BHB-CoA, we next implemented an in vitro assay, in which BHB and CoA were incubated with or without recombinant ACSS2 (fig. S10E), followed by LC-MS/MS analysis. As shown in Fig. 4H, BHB-CoA was readily detected in the presence of ACSS2, while it was almost lost with ACSS2 omitted. Furthermore, MS analysis confirmed the results (Fig. 4, H to J). The results indicate that ACSS2 is responsible for the conversion to BHB-CoA under BHB accumulation.

As ACSS2-mediated acetyl-CoA undergoes a two-step reaction by which a reactive acetyl-adenylate (acetyl-AMP) intermediate is formed in the first step (*35*, *36*), we speculate that ACSS2-dependent BHB-CoA may also produce BHB-AMP (Fig. 4G). On the basis of this, we performed docking analysis using ACSS2 and BHB-AMP to explore the underlying molecular basis for ACSS2 catalysis. The structural analysis showed that ACSS2 is able to accommodate BHB-AMP into a hydrophobic pocket wherein several key residues, such as T363, S317, T468, E469, and K661, potentiate the binding of ACSS2 to BHB-AMP through electrostatic and hydrogen-bonding interactions (fig. S11, A and B). We then performed mutagenesis experiments to determine the contribution of these residues and found that the T363A mutation markedly lowered histone Kbhb and H3K9bhb, whereas ectopic expression of WT-ACSS2 rather than the mutant rescued this reduction, verifying the essential role of these key residues of ACSS2 such as T363 for its catalysis (fig. S11, C and D). Moreover, an in vitro assay, in which BHB, CoA, and adenosine 5′-triphosphate (ATP) were incubated with recombinant ACSS2-WT or ACSS2-T363A (figs. S10E and S11E), was implemented, and the results further demonstrated that the residue T363 is crucial for ACSS2 to incorporate BHB into BHB-CoA (fig. S11, F and I). Together, we identified ACSS2 as the founding member of BHB-CoA synthetase and revealed the molecular mechanism by which ACSS2 fuels histone H3K9bhb through the local generation of BHB-CoA.

ACSS2 coupled with KAT7 modulates H3K9bhb across genome

To assess the chromatin occupancy of H3K9bhb and its correlation with KAT7 and ACSS2 in the genome, we performed CUT&Tag in BHB sodium (BHBNa)–treated cells, followed by high-throughput sequencing assays. Consequently, we identified 36918 H3K9bhb-, 29076 KAT7-binding–, and 12575 ACSS2-binding–enriched peaks in the genome. The occupancy of H3K9bhb (45.01%), KAT7 (50.76%), and ACSS2 (63.19%) was enriched at gene promoter regions (fig. S12, A to C). In total, 11040 KAT7-binding, 12586 H3K9bhb-binding, and 7061 ACSS2-binding gene promoter regions were identified. In addition, 6102 peaks that were cooccupied by KAT7, H3K9bhb, and ACSS2 were also identified (Fig. 5B). Furthermore, the heatmap plotting analysis showed that H3K9bhb, KAT7, and ACSS2 were strongly enriched at transcription start sites (TSSs) and adjacent regions of genes (Fig. 5A). The occupancy of them at TSSs was corroborated by the selected genes, such as *SAMD9* and *FRMD3* (Fig. 5, C and D). Notably, the average occupancies between H3K9bhb and KAT7 were higher than that of ACSS2-KAT7 and ACSS2-H3K9bhb (fig. S12, D to I), suggesting that KAT7 and ACSS2 may exert differing dynamics when dissociate from histone.

To test whether KAT7 is vital for H3K9bhb in the genome, we performed CUT&Tag in KAT7-deficient cells to analyze H3K9bhb-marked peaks. Notably, KAT7 depletion resulted in an obvious decrease in H3K9bhb occupancy on gene promoters (Fig. 5, E and F), of which 11,060 differential peaks were identified in KAT7-WT and KAT7-KO HeLa cells in the presence of BHBNa, implying the contribution of KAT7 to H3K9bhb bound on chromatin. Besides, most of these peaks were harbored within gene promoter regions and other intergenic regions, representing a wide distribution across the genome (fig. S12J). Specifically, a lower H3K9bhb enrichment on the selected genes was also observed owing to KAT7 loss, which was further confirmed by quantitative polymerase chain reaction (qPCR) assay (Fig. 5, G and H). These data indicated that KAT7 is instrumental for H3K9bhb in the genome, particularly within gene promoter regions. Last, GO analysis revealed that these genes with H3K9bhb modification regulated by KAT7 were mainly involved in cell migration and cell-cell junction, suggesting that KAT7-mediated H3K9bhb may regulate key genes representing cell mobility (fig. S12, K and L). Together, our findings show that KAT7 associated with ACSS2 regulates H3K9bhb across the genome, particularly in gene promoter regions.

ACSS2 coupled with KAT7 boosts histone Kbhb to regulate tumorigenesis-associated gene transcription

Given our findings that ACSS2 and KAT7 colocalize in chromatin and drive H3K9bhb in TSSs, we speculated that the established ACSS2-KAT7 module may regulate target gene transcription and functional outputs by promoting histone Kbhb. To test our hypothesis, we performed RNA-seq analysis in KAT7-depleted HeLa cells to identify candidate genes regulated by KAT7 and obtained 1501 down-regulated genes due to KAT7 loss under BHBNa stimulation (Fig. 6A and fig. S13A). Similarly, we also identified 1014 genes suppressed by ACSS2 inhibition in the presence of BHBNa treatment

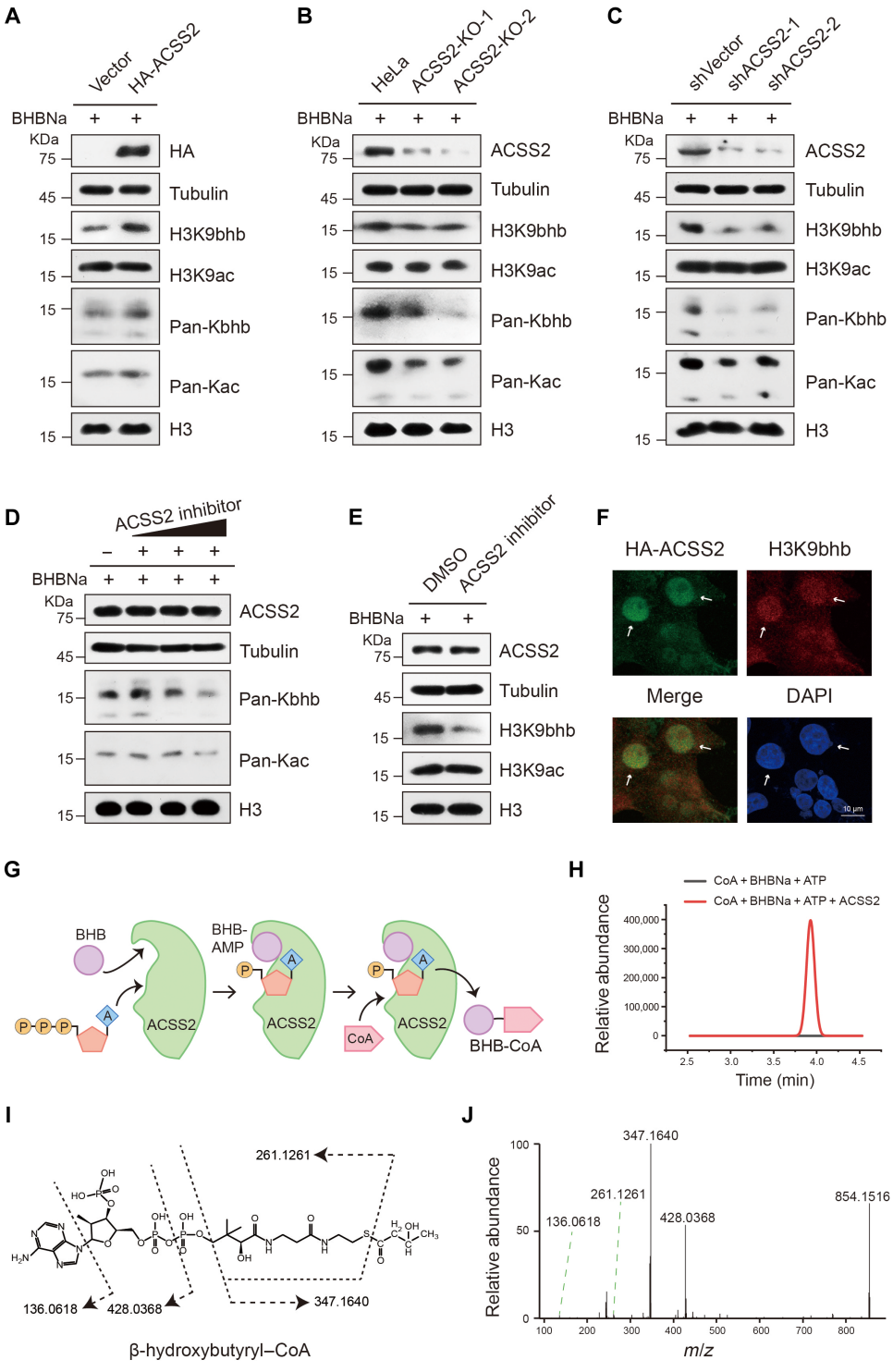

Fig. 4. ACSS2 uses BHB to generate the BHB-CoA and boosts histone β-hydroxybutyrylation. (**A**) WB analysis for pan-Kbhb and H3K9bhb on histones in HeLa cells overexpressing ACSS2. Histone acetylation used as a control. (**B** and **C**) Immunoblot analysis of Kbhb and H3K9bhb on histones in ACSS2-KO HeLa cells (B) or ACSS2-KD HepG2 cells (C). (**D** and **E**) Immunoblot assays for detecting the level of Kbhb and H3K9bhb on histones in HeLa cells pretreated with ACSS2 inhibitors. Immunoblot assays for (A) to (E) were in the presence of 10 mM BHBNa. (**F**) IF staining illustrating the increasing level of H3K9bhb in HeLa cells overexpressing ACSS2 upon BHBNa stimulation. (**G**) Schematic illustration showing the proposed catalytic mechanism of ACSS2-induced BHB-CoA. (**H**) Identification of BHB-CoA via high-performance LC (HPLC)–MS/MS analysis. The BHBNa was incubated with CoA and adenosine 5′-triphosphate (ATP) in the presence or absence of recombinant ACSS2, and the resulting sample was thereafter determined by HPLC-MS/MS. The *x* axis represents elution time, and the *y* axis represents ion relative abundance. (**I**) Illustration of the fragmentation pattern of BHB-CoA, which is drawn by ChemDraw (19.0). (**J**) The representative MS/MS spectrum of BHB-CoA detected from ACSS2-mediated acyl-CoA synthesis reaction in vitro. The *x* axis represents mass/charge ratio (*m/z*), and the *y* axis indicates ion relative abundance.

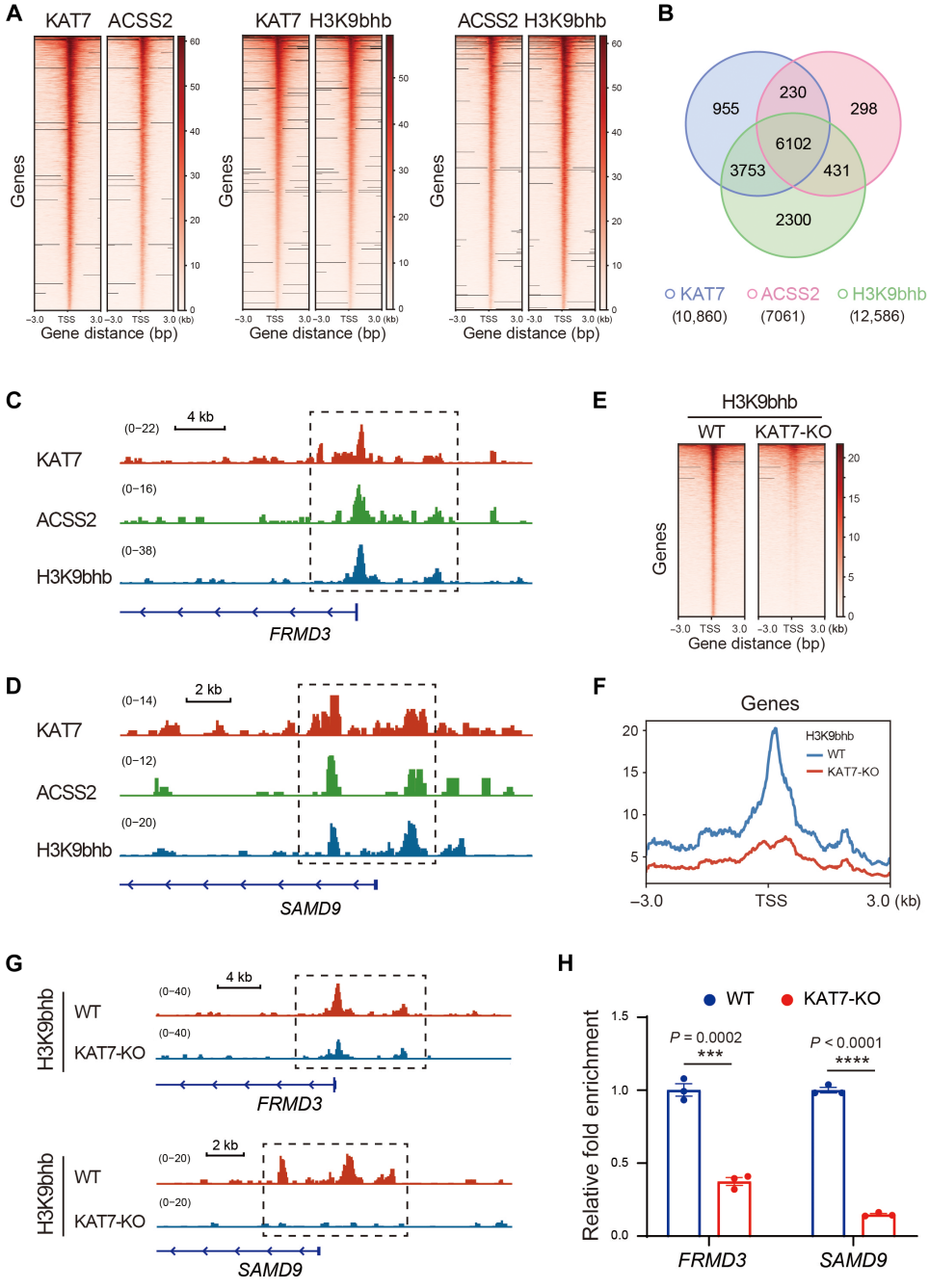

Fig. 5. KAT7 coupled with ACSS2 modulates H3K9bhb across genome. (**A**) Heatmap from CUT&Tag data analysis illustrates the distribution of KAT7, ACSS2, and H3K9bhb within ±3 kb of the TSS. Two biological replicates were performed for CUT&Tag. (**B**) Venn diagram showing the overlapped copeaks within ±3 kb of the TSS among KAT7-, ACSS2-, and H3K9bhb-enriched peaks. The overlapped part (green and blue parts) represents copeaks between KAT7 and H3K9bhb within ±3 kb of the TSS. The overlapped part (green and pink parts) represents copeaks between ACSS2 and H3K9bhb within ±3 kb of the TSS. The overlapped part (pink and blue parts) represents copeaks between KAT7 and ACSS2 within ±3 kb of the TSS. (**C** and **D**) Representative traces of *FRMD3* (left) and *SAMD9* (right) exhibiting enrichment of KAT7, ACSS2, and H3K9bhb within ±3 kb of the TSS. (**E** and **F**) Density of CUT&Tag reads (E) and averaged genome-wide occupancies (F) for H3K9bhb within ±3 kb of the TSS in KAT7-WT and KAT7-KO HeLa cells. (**G**) The trace of *FRMD3* (top) and *SAMD9* (bottom) displaying the distribution of differential peaks for H3K9bhb within ±3 kb of the TSS in KAT7-WT and KAT7-KO HeLa cells. (**H**) Target genes from CUT&Tag analysis, *FRMD3* and *SAMD9*, are further verified by chromatin immunoprecipitation (ChIP)–quantitative polymerase chain reaction (qPCR). The bar graph results showed the promoter levels enriched by H3K9bhb in KAT7-WT and KAT7-KO HeLa cells. Data are mean ± SEM ($n = 3$). ***$P < 0.001$ and ****$P < 0.0001$.

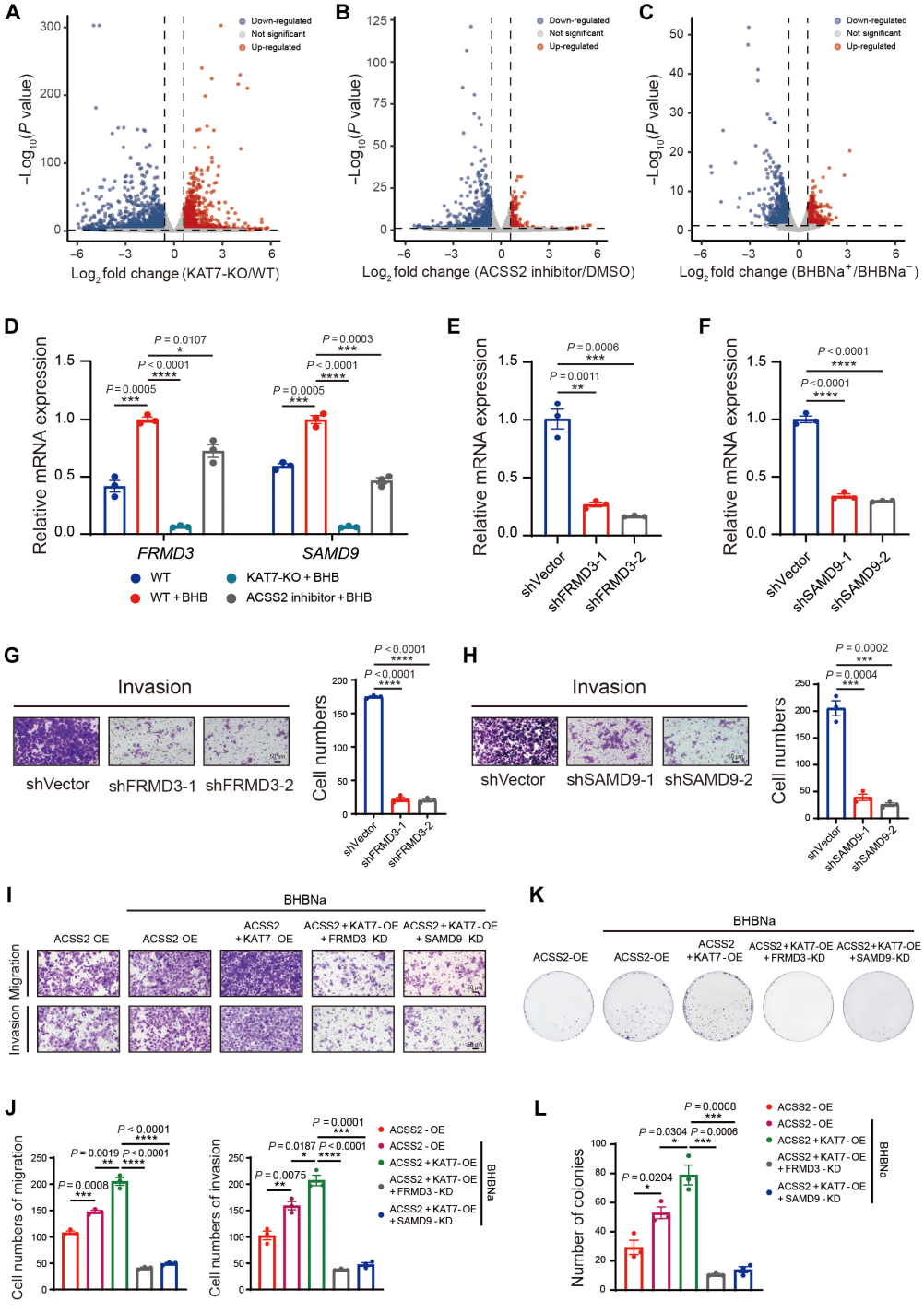

Fig. 6. KAT7 coupled with ACSS2 for specific regulation of tumorigenesis-related genes through histone Kbhb. (**A**) Volcano plot of RNA-seq analysis between KAT7-WT and KAT7-KO HeLa cells with BHBNa stimulation [1.5-FC cutoff, $P < 0.05$ ($n = 3$ in each group, from independent biological replicates)]. (**B**) Volcano plot of RNA-seq analysis showing cells treated with or without ACSS2 inhibitors under accumulation of BHBNa (1.5-FC cutoff, $P < 0.05$). DMSO, dimethyl sulfoxide. (**C**) Volcano plot of RNA-seq analysis for cells treated with or without BHBNa (1.5-FC cutoff, $P < 0.05$). (**D**) RT-qPCR analysis for the fluctuated mRNA level in WT cells with or without BHBNa treatment along with ACSS2 inhibitors or KAT7-KO cells with BHBNa stimulation. Data are mean ± SEM ($n = 3$). *$P < 0.05$, ***$P < 0.001$, and ****$P < 0.0001$. WT: cell control group without any treatment, WT + BHB: cells treated with BHBNa for 24 hours, KAT7-KO + BHB: KAT7-KO cells treated with BHBNa for 24 hours, and ACSS2 inhibitors + BHB: cells treated with ACSS2 inhibitors and BHBNa for 24 hours. (**E** and **F**) The relative mRNA levels illustrating the KD efficiency of *FRMD3* and *SAMD9*. Data are mean ± SEM ($n = 3$). *$P < 0.05$, **$P < 0.01$, ***$P < 0.001$, and ****$P < 0.0001$. (**G** and **H**) The transwell invasion assay showing the inhibition of invasion behavior of HeLa cells after FRMD3 (left) and SAMD9 (right) KD. ***$P < 0.001$ and ****$P < 0.0001$. (**I** and **J**) The migration and invasion assays demonstrating the effect of BHB-driven "ACSS2-KAT7-H3K9bhb" axis through detecting the rate of migration (top) and invasion (bottom). OE, overexpression. **$P < 0.01$, ***$P < 0.001$, and ****$P < 0.0001$. (**K** and **L**) The clone formation assay showing BHB-driven ACSS2-KAT7 module having an effect on cell clonogenicity requiring H3K9bhb. *$P < 0.05$ and ***$P < 0.001$.

(Fig. 6B and fig. S13B). Furthermore, we aimed to detect histone Kbhb–mediated genes by comparing the RNA-seq assay in cells with or without BHB and found that 631 genes were up-regulated by BHB induction (Fig. 6C and fig. S13C). The GO analysis demonstrated that the genes regulated by KAT7, ACSS2, or BHB induction were involved in several critical pathways, including the regulation of transcription activity and metabolic processes, suggesting that KAT7 and ACSS2 may act through the coregulation of these genes (fig. S13, E to G). We therefore considered one gene as a candidate target, regulated by BHB-driven "ACSS2-KAT7" module, with features that its expression was blocked by KAT7 depletion and ACSS2 inhibition and induced by BHB. Consequently, 13 genes that satisfied the criteria were identified, and their transcript levels were further verified by reverse transcription qPCR (RT-qPCR) analysis (Fig. 6D and fig. S13, D and H), suggesting that the ACSS2-KAT7 module drives specific gene transcription by regulating histone Kbhb. Notably, *SAMD9* and *FRMD3* were highly cooccupied by KAT7, ACSS2, and H3K9bhb at promoter regions and regarded as downstream targets activated by KAT7-induced H3K9bhb (Fig. 5, C, D, G, and H). In addition, *SAMD9* and *FRMD3* may promote postoperative recurrence of esophageal squamous cell carcinoma and breast cancer (*37*, *38*); however, their functions in cervical cancer remain unknown. Collectively, these two genes were considered to be key targets regulated by the ACSS2-KAT7-H3K9bhb axis.

To address the functions of genes regulated by the ACSS2-KAT7-H3K9bhb cascade, we first analyzed the effects of shRNA-mediated KD of FERM domain containing 3 (FRMD3) and sterile alpha motif domain containing 9 (SAMD9; Fig. 6, E and F) in HeLa cells. Notably, FRMD3 depletion significantly lowered cell proliferation, migration, invasion, and clonogenicity (Fig. 6G and fig. S14, A, C, E, and F). Similarly, KD of SAMD9 also inhibited malignant behaviors (Fig. 6H and fig. S14, B, D, G, and H). To further verify SAMD9/FRMD3 as key targets of the ACSS2/KAT7/H3K9bhb axis in mediating tumor cell growth, we performed an array of phenotypic experiments (Fig. 6, I to L, and fig. S14, I and J). Consequently, the cells expressing ACSS2 plus KAT7 showed an elevated cell proliferation compared to cells expressing ACSS2, indicating a synergic role of ACSS2/KAT7 in regulating tumorigenesis. Notably, SAMD9/FRMD3 depletion significantly decreased cell growth despite the overexpression of ACSS2/KAT7, indicating that *SAMD9*/*FRMD3* are key targets regulated by the ACSS2/KAT7 axis. BHB induction markedly increased cell proliferation in cells transfected by ACSS2, confirming a critical function contributed by histone Kbhb (Fig. 6, I to L, and fig. S14, I and J). These results revealed that KAT7-linked ACSS2 mediates tumorigenesis-related gene expression via regulation of histone Kbhb. Collectively, our data unveil a proposed model that ACSS2 senses cellular BHB and translocates into the nucleus, wherein it binds to KAT7 and colocalizes with it at gene promoters. Moreover, KAT7 acts as histone β-hydroxybutyryltransferase to boost histone Kbhb using ACSS2-generated BHB-CoA, thereby driving oncogenic gene transcription (Fig. 7).

DISCUSSION

Kbhb is an epigenetic mark that links ketogenic metabolism to gene transcription. Recently, it has been shown that ketogenesis-generated BHB functions as a chromatin regulator through promoting Kbhb modification on histones (*10*). However, the molecular mechanism by which BHB is converted to BHB-CoA, the cofactor for histone Kbhb, remains unknown, representing an important gap in this PTM and epigenetic pathway. In this study, we report that ACSS2 functions as a BHB-CoA synthetase, and KAT7 serves as a histone β-hydroxybutyryltransferase. We further propose the BHB-driven ACSS2-KAT7 module, in which BHB induces ACSS2 translocation into the nucleus wherein ACSS2 interacts and colocalizes with KAT7 at gene promoters to boost specific histone Kbhb, providing a BHB-ACSS2-KAT7-H3K9bhb axis for elucidating the regulatory mechanism of histone Kbhb and highlighting the linkage of ketone metabolism and epigenetic regulation.

It has been uncovered that ACSS2 enables translocation to nucleus under glucose deprivation (*29*). However, whether ACSS2 can sense cellular BHB remains unclear. In this study, we found that BHB induced pS267 on ACSS2, which, in turn, promotes its nuclear translocation and interaction with KAT7 in the nucleus. This allows the BHB-CoA produced locally by ACSS2 to be neighboring with KAT7, thereby providing the concentrated BHB-CoA for KAT7 in the local chromatin. Typically, acyl-CoA (e.g., crotonyl-CoA and BHB-CoA) is present throughout the cell and is at about 1000-fold lower concentration than acetyl-CoA, which is far below the dissociation constant (K_d) of HATs (*39*–*41*). Hence, HATs are likely incapable of using this acyl-CoA on a global level, whereas offering a locallyfv concentrated acyl-CoA may be an alternative solution for this. Our study unveils a BHB-driven ACSS2-KAT7 module, by which the BHB-CoA generated by ACSS2 fuels local chromatin via KAT7 to boost histone H3K9bhb instead of H3K9ac due to local BHB-CoA accumulation, albeit of a globally low level of BHB-CoA in the nucleus. This, in turn, supports the specific activation of tumorigenesis-associated genes and cell proliferation. Of note, we identified 1014 genes that were modulated by ACSS2, of which 13 genes were coregulated by KAT7, ACSS2, and BHB, representing about 1% of ACSS2-manipulated genes. Gene transcription regulation by the BHB-driven ACSS2-KAT7 axis necessitates the cooperation of BHB, ACSS2, and KAT7 at a specific gene locus, implying that a small proportion of genes regulated by ACSS2 alone could be primary targets of the axis, whereas most genes manipulated by ACSS2 may be attributed to its contribution to the acetyl-CoA pool and different complexes that it is involved in (e.g., KAT8 or KAT2A) (*32*, *33*, *42*, *43*). These results may represent a spatiotemporal regulatory paradigm where cellular metabolites (e.g., acetate, BHB, or lactate), metabolic enzymes, and HATs are coupled at specific chromatin loci for orchestrating histone modification along with gene expression. HATs are canonical writers that transfer acetyl groups to histone lysine residues (*24*). Recently, the HAT p300 has been shown to install the BHB moiety on histones (*23*), representing the only known writer of Kbhb. Whether there are other enzymes responsible for Kbhb installation remains elusive. Here, we showed that KAT7 can catalyze the generation of lysine β-hydroxybutyration in vitro and in cells through genetic and biochemical analyses, expanding the repertoire of Kbhb transferases. Using a quantitative proteomics approach, we identified hundreds of KAT7-regulated Kbhb sites of substrate proteins including histone and nonhistone proteins, among which H3K9bhb showed the most significantly changed level, indicating that KAT7 may prefer to modulate Kbhb of histones. This is similar to the fact that KAT7 favors histone acetylation, relying on its scaffold proteins (*26*). Besides, it is well recognized that HATs use acyl-CoA to deposit lysine acylation on their potential substrates (*44*), akin to BHB-CoA for KAT7, but it remains unclear as to how BHB-CoA is produced in cells presently. Here, we revealed that ACSS2 is capable of catalyzing BHB-CoA

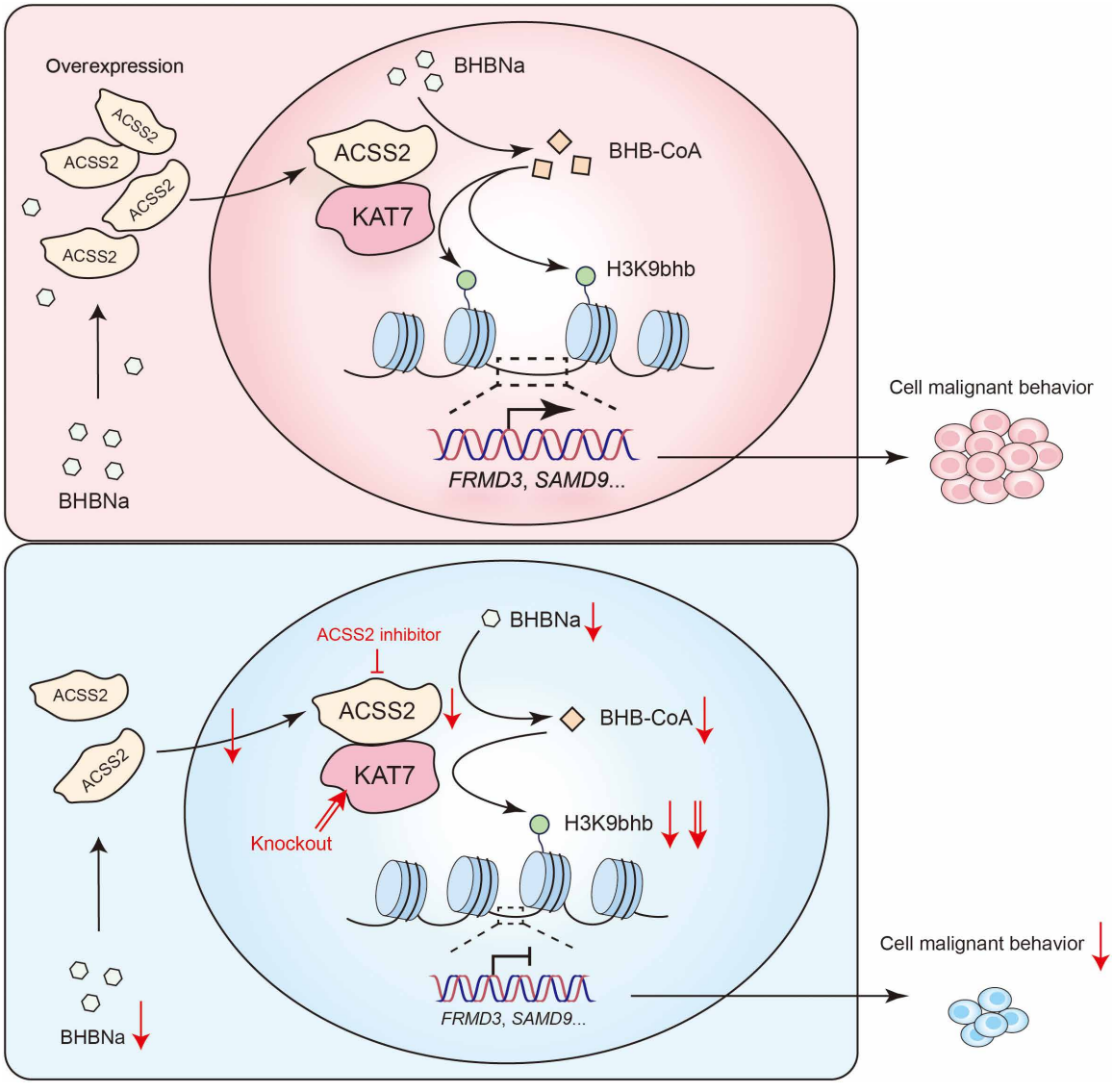

Fig. 7. Graphic model as described in the text. BHB-driven ACSS2-KAT7 module mediates histone H3K9bhb to boost transcription.

via the ligation of BHB to CoA by leveraging an in vitro assay and structural analysis.

Although our study revealed that the ACSS2-KAT7 module drives H3K9bhb, gene transcription, and tumorigenesis, we also identified other KAT7-regulated Kbhb sites on histones and nonhistones. Future studies to investigate the functional involvement of these Kbhb marks in tumorigenesis are necessary to better understand this module. Besides, although we found that BHB-induced pS267 on ACSS2 enables it to sense cellular BHB and translocate into the nucleus, the precise mechanism by which BHB promotes ACSS2 phosphorylation remains to be further explored.

In conclusion, we identify ACSS2 as the founding member of BHB-CoA synthetase and KAT7 as a histone β-hydroxybutyryltransferase. We show that BHB-driven ACSS2 is recruited by KAT7 to coregulate histone H3K9bhb for transcription of oncogenic genes. Our findings provide mechanistic insights into how BHB precisely drives specific histone Kbhb, filling an important gap in the histone Kbhb pathway.

MATERIALS AND METHODS

Cell culture

Human HeLa, HEK-293T, and HepG2 cells were cultured in Dulbecco's modified Eagle's medium (DMEM; VivaCell). The medium was supplemented with 1% penicillin/streptomycin and 10% fetal bovine serum (FBS) (VivaCell, Shanghai, China) for HeLa, HEK-293T, and HepG2 cells. All cells were cultured at 37°C in a humidified atmosphere with 5% CO_2. The cells were cultured in DMEM with 5 or 10 mM BHBNa referring to the literature about the biological functions of a ketone body (*6*, *45*). The details for reagents in this paper can be found in table S6.

Plasmids and established stable cells

All shRNA and single guide RNA (sgRNA) used were purchased from GENEWIZ. After oligonucleotides annealed, the double-strand oligos were cloned into pLKO.1-Puro or lentiCRISPR v2, followed by cotransfection with pMD2.G and psPAX2 into HEK-293T cells.

The HeLa, HEK-293T, or HepG2 cells were incubated with virus targeted at genes (KAT7, ACSS2, FRMD3, and SAMD9) and then selected with puromycin (2 μg/ml) to establish stable cells. Moreover, two kinds of stable KAT7-KO cell lines (KAT7-KO-1 and KAT7-KO-2) in our study were obtained from our laboratory.

CRISPR-Cas9 KO and shRNA KD

Following procedures previously described in (*46*), we established the KAT7- or ACSS2-deficient cell lines. Briefly, targeted sgRNA was incorporated into the lenti-CRISPR v2 vector and then cotransfected into HEK-293T cells with psPAX2 and pMD2.G plasmids to produce the corresponding virus. After cells were infected with the virus for 24 hours, purinomycin drug (2 μg/ml) was added to select cells until no cells were dead. For shRNA KD, analogously, the shRNA of the target gene was also incorporated into the pLKO.1-Puro vector, and the other processes were identical to those in CRISPR-Cas9 KO mentioned above. All sequences of sgRNA and shRNA involved in this paper can be obtained in table S4.

WB assays

Protein samples were separated with 8, 12, or 15% SDS–polyacrylamide gel electrophoresis (SDS-PAGE) gel and then transferred to a nitrocellulose filter membrane, which was blocked with 5% nonfat powdered milk at room temperature for 2 hours and incubated with primary antibody at 4°C overnight. The membrane was washed three times with tris buffered saline with Tween-20 [20 mM tris-HCl (pH 7.6), 150 mM NaCl, and 0.1% Tween 20] and then incubated with the secondary antibody for 2 hours at room temperature. Last, the film on top of the blot was placed with the film edge for the desired exposure time, and then the film was gently removed and immediately fed into the Exomat (*46*).

IF staining

As described in our previous work (*46*), HeLa cells were washed three times with phosphate-buffered saline (PBS) on the coverslips and then fixed at room temperature with 4% paraformaldehyde (PFA) for 30 min. Cells were permeabilized with 0.5% Triton X-100 at room temperature for 15 min and blocked with 5% bovine serum albumin for 1 hour. The cells were incubated with the corresponding primary antibody at 4°C overnight. After being washed three times with PBS, the fluorescent secondary antibody was incubated at room temperature for 1 hour. Subsequently, the samples were incubated with fluorescent mounting medium with 4′,6-diamidino-2-phenylindole (DAPI) at room temperature for 5 min for staining and sealing. In the end, the microscopic images were captured using an Axio Imager LSM 900 microscope.

Acid extraction of histones

Histones were extracted using a standard extraction protocol (*46*). To begin with, cells were collected and washed twice with precooled PBS containing 5 mM sodium butyrate. After centrifugation, the supernatant was discarded. Then, cells were dissolved with 1 ml of Triton extraction buffer [0.5% Triton X-100, 1 mM protease inhibitor cocktail, 1 mM phenylmethylsulfonyl fluoride (PMSF), and 5 mM sodium butyrate dissolved in PBS solution] solution buffer, and the solution was transferred into a 1.5-ml centrifuge tube on ice for 10 min before centrifuging and discarding supernatant. HeLa cells were washed with half the volume of Triton extraction buffer again. Next, 0.2 M H_2SO_4 was supplemented and incubated with protein at 4°C overnight. The samples were centrifuged at 4°C for 10 min, and the supernatant was transferred to another 1.5-ml tube. Trichloroacetic acid (TCA) solution (50%) was mixed with the protein solution. After centrifuging and discarding the supernatant, the histone was washed three times with 100% acetone, and then the samples were stored at −20°C.

Histone β-hydroxybutyrylation reaction in vitro

Histone β-hydroxybutyrylation assay in vitro was conducted as described previously, and histones were used as substrates according to the protocol for histone extraction (*46*). Briefly, 200 μM BHB-CoA, 4 μg of histone, and 2 μg of enzyme (KAT7 catalytic domain) were coincubated in a reaction buffer [25 mM tris-HCl (pH 8.0), 150 mM NaCl, 10% glycerol, 1 mM sodium butyrate, and 1 mM dithiothreitol (DTT)] at 37°C following a time gradient. Last, the reaction was terminated with 2× SDS loading buffer, and the acylation of histone was determined by WB.

SILAC and sample preparation

The procedures of SILAC were described in our previous work (*46*). Respectively, WT and KAT7-KO HeLa cells were cultured in DMEM containing L-arginine and L-lysine (100 mg/ml) (KAT7-KO) or L-arginine and $^{13}C_6$-lysine (WT). After evaluating that the labeling efficiency was more than 98%, all cells were treated with 10 mM BHBNa and then harvested. Furthermore, histones and plasmosin were extracted from cells. Proteins (histones or plasmosin) were equally mixed and precipitated with TCA. Then, the precipitated proteins were digested using trypsin (1:50) at 37°C overnight in 100 mM NH_4HCO_3. The digested peptides were added with 5 mM DTT and then incubated for 1 hour at 56°C. Iodoacetamide (15 mM) was also added under darkness for 45 min, and then 30 mM cysteine was incubated at room temperature for 30 min, followed by secondary digestion with trypsin (1:100) at 37°C for 4 hours. The final product was desalted by Sep-Pak C18 cartridges (Waters) and subsequently drained by the SpeedVac system (Thermo Fisher Scientific).

Immunoaffinity enrichment for β-hydroxybutyrylation peptides

After samples were desalted and drained for immunoaffinity enrichment, they were subsequently dissolved with NETN buffer [50 mM tris-HCl (pH 8.0), 100 mM NaCl, 1 mM EDTA, and 0.5% Nonidet P-40], followed by incubation with prewashed anti–BHB lysine antibody-conjugated protein A agarose beads (PTM Biolabs) overnight at 4°C. The incubated beads were washed three times with NETN buffer, twice with ETN buffer [50 mM tris-HCl (pH 8.0), 100 mM NaCl, and 1 mM EDTA], and once with high-performance LC (HPLC) grade H_2O. Bound beads were eluted three times with 1% trifluoroacetic acid. Last, the elution was drained and cleaned by C18 ZipTips (Millipore Corporation), followed by nano–HPLC-MS/MS analysis according to the procedures in our previous work (*46*).

HPLC-MS/MS analysis for Kbhb

Modified peptides were further analyzed by HPLC-MS/MS (*46*). Briefly, each sample of enriched Kbhb peptides was reconstituted in 0.1% formic acid and then injected into a nano-LC system (EASY-nLC 1200, Thermo Fisher Scientific). Peptides were resolved in a C18 column (75-μm inner diameter ×25 cm, 3-μm C18) over 130 min at a flow rate of 300 nl/min. The HPLC gradient was as follows: 5 to 7% solvent B (0.1% formic acid in 80% acetonitrile) in 2 min, 7 to 22%

solvent B in 78 min, 22 to 38% solvent B in 38 min, 38 to 100% solvent B in 3 min, and hold for 9 min at 100% solvent B. An Orbitrap Eclipse Tribrid mass spectrometer supplied with a FAIMS Pro Duo (Thermo Fisher Scientific) was used for MS analysis. Spray voltage was set to 2.2 kV, funnel radio frequency (rf) lens level at 40%, and ion transfer tube temperature at 320°C. Combination of different FAIMS compensation voltages was set to run data-dependent acquisition (DDA) mode of the most intense precursors for a 1-s cycle to build a big cycle of 2 s, and data were collected by Xcalibur (v.4.5).

Data processing

The data search and filter criteria were performed as described in (*46*): The UniProt human proteome database was applied for the search by MaxQuant (v.1.5.5.1), with an overall FDR (false discovery rate) for peptides of less than 1%. The main search parameters were as follows: trypsin as the proteolytic enzyme; two permitted missed cleavages; seven amino acid residues as minimal peptide length; carbamidomethylation on cysteine as a fixed modification; oxidation of methionine, acetylation on the peptide N terminus, and Kbhb as variable modifications; and mass error of ±10 parts per million (ppm) for precursor ions and ±0.02 kDa for fragment ions. To improve the accuracy of β-hydroxybutyrylated peptide identification, we further excluded peptides with a score of <40 or localization probabilities <0.75. The ratio of quantified Kbhb peptide was further normalized by their corresponding protein levels.

Co-IP assay

For in vivo Co-IP, HeLa cells were cultured in medium until cell population density reached 70%. Subsequently, plasmids of KAT7 and ACSS2 were cotransfected into HeLa cells for 48 hours. Cells were then harvested, washed twice with PBS, and lysed with IP buffer [50 mM tris-HCl (pH 7.5), 150 mM NaCl, 0.2% NP-40, 1 mM PMSF, and 1 mM protease inhibitor cocktail]. Cell extracts were incubated with precleared protein A + G agarose (Beyotime) at 4°C for 6 hours. The supernatants were then incubated respectively with antibodies against ACSS2, KAT7, immunoglobulin G (IgG), and A + G agarose overnight at 4°C, followed by washing the beads four times with cold Co-IP buffer. The beads were then added to the loading buffer and boiled at 95°C for 10 min. Last, the supernatants were subjected to SDS-PAGE and WBs.

Glutathione *S*-transferase pull-down assay

For the pull-down assay, we first purified the recombinant glutathione *S*-transferase (GST) vector and GST-ACSS2 from *Escherichia coli*, followed by incubation with GST beads (GE HealthCare) for 4 hours. Subsequently, cells were harvested and lysed with GST pull-down buffer (PD buffer) [20 mM tris-HCl (pH 7.5), 100 mM NaCl, 0.1 mM EDTA, and 0.2% Triton X-100] after the Flag-KAT7 plasmid was transfected into cells for 48 hours. The supernatant containing Flag-KAT7 was divided equally into the GST vector and GST-ACSS2 for incubation overnight. The beads were washed three times with PD wash buffer [20 mM tris-HCl (pH 7.5), 300 mM NaCl, 0.1 mM EDTA, and 0.5% Triton X-100]. Last, the samples were heated at 95°C for 10 min, followed by the detection of WB analysis.

LC-MS/MS and IP-MS analysis

Following procedures previously described in (*47*), the LC-MS/MS or IP-MS analysis was conducted. For LC-MS/MS analysis, peptides were dissolved in 0.1% formic acid (FA) and directly loaded onto a reversed-phase precolumn (Acclaim PepMap 100, Thermo Fisher Scientific). Peptide separation was performed using a reversed-phase analytical column (Acclaim PepMap RSLC, Thermo Fisher Scientific). The standard parameters commonly used in HPLC-MS/MS proteomics were performed. Specifically, the HPLC gradient elution for sample separation was performed by an increase from 5 to 22% solvent B (0.1% FA in 98% acetonitrile) for 41 min, 22 to 38% for 23 min, climbing to 100% in 3 min, and then holding at 100% for 8 min, all at a constant flow rate of 280 nl/min on an EASY-nLC 1000 UPLC system. The resulting peptides were injected into an Nano Spray Ionization source, followed by MS/MS analysis in an Orbitrap Eclipse Tribrid mass spectrometer (Thermo Fisher Scientific). Intact peptides were detected in the Orbitrap at a resolution of 60,000. For MS scans, the mass/charge ratio (*m/z*) scan range was 400 to 1200. A data-independent acquisition procedure was performed with the setting parameters. The resulting MS/MS data were processed using Spectronaut. Tandem mass spectra were searched against UniProt human database (downloaded on 24 November 2023) concatenated with a reverse decoy database. Trypsin/P was specified as a cleavage enzyme allowing up to two missing cleavages. The mass error was set to 10 ppm for precursor ions and 0.02 kDa for fragment ions. Carbamidomethylation on cysteine was specified as a fixed modification, and oxidation on Met and acetylation on the protein N-terminus were specified as variable modifications. FDR thresholds for protein, peptide, and modification sites were specified at 1%. The minimum peptide length was set at 7, and "match between runs" was enabled. All the other parameters in Spectronaut were set to default values.

For IP-MS analysis, the plasmids of KAT7 or empty vector were overexpressed in HeLa cells for 48 hours, followed by the stimulation of BHB for 24 hours. The cells were then collected and placed on ice in IP buffer for 20 min. Anti-Flag agarose beads were incubated with cell extract at 4°C for 4 hours. The beads were washed three times with IP buffer. Next, the beads were resuspended with 100 mM NH_4HCO_3 solution, followed by supplementation with 5 mM DTT at 56°C for 1 hour, 15 mM iodoacetamide at room temperature for 45 min, and 30 mM cysteine for 30 min. The samples were digested with trypsin (1:50) at 37°C overnight. The sample was dissolved in 0.1% trifluoroacetic acid and then subjected to HPLC-MS/MS analysis using an Orbitrap Eclipse Tribrid mass spectrometer (Thermo Fisher Scientific). In turn, the HPLC gradient was as follows: 5 to 6% solvent B (0.1% formic acid in 80% acetonitrile) in 2 min, 6 to 28% solvent B in 87 min, 28 to 40% solvent B in 26 min, 40 to 100% solvent B in 10 min, and held for 5 min at 100% solvent B. The scan range (*m/z*) was 350 to 1500, and the DDA mode was applied. The results were further analyzed for Proteome Discoverer (Thermo Fisher Scientific). In detail, the UniProt human database (downloaded on 24 November 2023) was applied for the search. Two missed cleavages were set, six amino acid residues as minimal peptide length, carbamidomethylation on cysteine as a fixed modification, oxidation of methionine, acetylation on the peptide N terminus as variable modifications, and mass error of ±10 ppm for precursor ions and ±0.02 kDa for fragment ions.

For identification of phosphorylation on ACSS2 via IP-MS/MS analysis, cells expressing Flag-ACSS2 were cultured for 48 hours, followed by BHB stimulation for 24 hours. Then, the cells were harvested and lysed, and the supernatant was incubated with anti-Flag agarose beads, followed by preparation of samples for HPLC-MS/MS analysis. The results were further analyzed using MaxQuant (v.1.5.5.1). The detailed parameter settings were as previously mentioned. In particular,

the phosphorylation was set as a variable modification besides oxidation of methionine and acetylation on the peptide N terminus.

Recombinant protein expression and purification

The recombinant protein expression and purification were performed to verify the catalytic activity of KAT7 and ACSS2. Plasmids of KAT7 (336 to 611)–pET28a and full-length ACSS2-PET28a were transferred into *E. coli* BL21 (DE3) and cultured in LB medium containing kanamycin (50 μg/ml) in a 37°C shaker until the optical density $(OD)_{600}$ value reached 0.6 to 0.8. Isopropyl-β-D-thiogalactopyranoside (final concentration of 0.5 mM) was then added, continuing to culture at 16°C overnight. Lysis of *E. coli* was conducted by an ultraphonic crusher and then centrifuged at 12,000 rpm at 4°C for 30 min. The supernatant was incubated with HisPur Ni–nitrilotriacetic acid resin (Cytiva), and the recombinant protein was bound with Ni resin. After washing beads three times with washing buffer, proteins were subsequently eluted. Eluted proteins were frozen in liquid nitrogen and then stored at −80°C for relevant reactions in vitro.

In vitro assay for ACSS2 activity

Assay of the acyl-CoA synthetase activity of ACSS2 was executed as previously described protocols with a slight adjustment (*48*, *49*). Briefly, the enzyme reactions were carried out in 70 mM tris-HCl (pH 7.9) buffer, containing 2 mM CoA, 8 mM ATP, 2 mM BHB, 5 mM KCl, and 4 mM $MgCl_2$ at 37°C for 1 hour and initialized by adding 7.5 μg of purified ACSS2. The total volume of the reaction mixture was 50 μl. The mixtures were preincubated at the designated reaction temperature for 5 min before the initiation. The reactions were terminated by adding an equal volume of 10% (v/v) trifluoroacetic acid and centrifugation, the supernatant was cleaned with C18 ZipTips, and the products of BHB-CoA were detected by LC-MS/MS.

HPLC-MS/MS analysis for BHB-CoA and acetyl-CoA

Identification of acyl-CoA was performed as described previously (*48*). Briefly, samples were separated by an ACQUITY UPLC BEH C18 column (2.1 mm by 100 mm, 1.7 μm); the HPLC gradient for 15 min was performed as follows: flow (0.2 ml/min) at 98% buffer A (water with 5 mM ammonium acetate) and 2% buffer B (95% acetonitrile in water with 5 mM ammonium acetate) for 0 min, 98 to 70% buffer A for 8 min, 70 to 2% buffer A for 1 min, 2% buffer A for 3 min, 2 to 98% buffer A for 1 min, and 98% buffer A for 2 min. An Orbitrap Exploris 480 (Thermo Fisher Scientific) was used for MS analysis. Spray voltage was set to 3.5 kV, funnel rf level at 40, and ion transfer tube temperature at 320°C. Data were collected by Xcalibur (v.4.0.27.19). The Orbitrap mass analyzer was used as the MS1 detector with 120,000 resolution. The normalized Automatic Gain Control target and maximum injection time were set at 70% of the standard for MS1. The MS2 detector was used at a resolution of 15,000. Targeted mass setting is BHB-CoA: 854.1516 and acetyl-CoA: 810.1330. MS2 isolation window was 2 kDa, mass tolerance was 10 ppm, and a normalized HCD (higher-energy collision-induced dissociation) collision energy of 25% was used for precursor fragmentation. The relative intensity of acyl-CoA was analyzed by Xcalibur (v.4.0.27.19).

Molecular docking

Following procedures previously described in (*46*), we implemented the molecular docking analysis. First, both the chemical formula of Bhb-AMP and the structure of BHB-CoA [chemical entities of biological interest (ChEBI) ID: 15452] were retrieved in simplified molecular input line entry system (SMILES) format from the ChEBI (www.ebi.ac.uk/chebi/) database. Subsequently, the format of two ligands was then converted into Protein Data Bank (PDB) format using the software Chem3D for further molecular docking. PDB formats of KAT7 (PDB: 6MAJ) and ACSS2 were respectively downloaded from PDB (www.rcsb.org) and AlphaFold Protein Structure Database (https://alphafold.ebi.ac.uk/entry/Q9NR19) as the receptor proteins. To perform molecular docking of ligand with proteins, the Surflex-Dock module was used in our in silico study and then traced out the feature of the calculation of grid maps automatically. After the successful docking, confirmation of the binding position of the ligand into the receptor proteins and calculation of bond distance were also conducted by PyMOL (www.pymol.org) and LigPlus.

CUT&Tag

CUT&Tag was performed using the Hyperactive Universal CUT&Tag Assay Kit for Illumina (TD903-01, Vazyme Biotech) in accordance with the procedures described in (*46*). Briefly, WT and KAT7-KO HeLa cells were collected and counted for incubation with pretreated Concanavalin A beads. Cells were then resuspended in an antibody buffer and incubated overnight at 4°C with the corresponding primary antibody of KAT7, H3K9bhb, or ACSS2. The secondary antibodies were added in appropriate proportions and incubated with the cells at room temperature. Subsequently, pA/G-Tnp transposons were rotated and incubated with the samples for 1 hour to activate the translocase, fragment DNA, and extract DNA. The DNA library was constructed with TruePrep Index Kit V2 for Illumina (TD202, Vazyme Biotech). The library was purified by VAHTS DNA Clean Beads (N411, Vazyme Biotech) and sequenced by Illumina NovaSeq 150PE (all data from CUT&Tag experiments were replicated twice).

CUT&Tag data processing and normalization

The detailed process of bioinformatics analysis of CUT&Tag data was referring to our previous analysis procedures (*46*): The sequencing quality was evaluated by FastQC version (v0.11.9). First, all reads were aligned to the human genome build hg38 using Bowtie2 (v2.4.5) with the default parameters. Duplicate reads were removed using Picard tools (version 2.27.4). SAMtools version (1.15.1) was then used to convert and sort files to binary alignment map (BAM) format. Subsequently, uniquely mapped reads were normalized using deepTools (version 3.5.1) with the parameters: –normalize Using RPKM --binSize 50, to visualize CUT&Tag signals at specific genomic loci by Integrative Genomics Viewer (IGV; version 2.15.1). In the end, peaks were identified for each sample and biological replication using Model-based Analysis of ChIP-Seq version 2 (MACS2; version 2.2.7.1) with command-line options: "macs2 callpeak -q 0.05 -g hs -f BAM --nomodel".

Chromatin immunoprecipitation-qPCR

For chromatin immunoprecipitation (ChIP)–qPCR, an appropriate amount of WT and KAT7-KO HeLa cells was harvested after treatment with BHB for 24 hours. The cross-linking was then carried out by adding formaldehyde for 10 min and immediately terminated by adding glycine. After cells were permeabilized by swelling buffer [25 mM tris-HCl (pH 7.9), 1.5 mM $MgCl_2$, 10 mM KCl, and 0.1% NP-40], the samples were sheared by micrococcal nuclease at 37°C, and then the cells were further sonicated on ice. The sonicated chromatin was subsequently subjected to IP with the according antibodies

H3K9bhb and protein A + G agarose (Beyotime). After extensive washing, the eluted DNA-protein complexes were de–cross-linked at 65°C overnight, followed by digestion with Proteinase K (Invitrogen) at 55°C for 2 hours and RNase A (Roche) at 37°C for 1 hour. At last, the DNA was purified with ethanol precipitation and then quantified by qPCR.

RNA-seq analysis

The clustering of samples was performed on a cBot Cluster Generation System using TruSeq PE Cluster Kit v3-cBot-HS (Illumina) according to the manufacturer's instructions. After cluster generation, the library preparations were sequenced on an Illumina NovaSeq platform, and 150–base pair (bp) paired-end reads were generated. Next, gene expression levels were calculated by expectation maximization, and differentially expression genes were identified by DESeq2 algorithms based on gene expression levels. Fold change ≥ 1.5 and $P < 0.05$ were selected as substantially differentially expression genes (*50*, *51*). Each experiment was analyzed with three biological replicates for statistical analysis.

Reverse transcription qPCR

For RT-qPCR, total RNA of cells was extracted by the standard TRIzol extraction method, followed by cDNA synthesis of 1 μg of RNA using StarScript III All-in-one RT Mix with gDNA Remover Kit (GenStar) as described in (*46*). SYBR-Green–based qPCR was performed to measure the expression of genes. The mRNA expression level was normalized by the expression level of glyceraldehyde-3-phosphate dehydrogenase. All sequences for ChIP-qPCR and (RT)-qPCR in this paper can be obtained in table S5.

Cell clonal formation assays

After cells were counted, 1000 cells per well were inoculated into the 12-well culture plate, and the medium was discarded every 3 days. After culturing for 1 week, the cells were washed twice with PBS and fixed with 1 ml of 4% PFA for 30 min. They were then stained with crystal violet solution for 10 min, followed by washing twice with PBS. The formation of cell clones was photographed.

Wound healing assays (detection of migration of cells)

Following procedures previously described in (*46*), the cell layer was scratched with a sterile pipette tip after they were monolayered on a six-well plate. Cells were replaced with fresh serum-free medium and cultured in a 37°C, 5% CO_2 incubator. After scratching for 0, 24, and 48 hours, the cells at the same location were recorded with a microscope. Last, the results were analyzed by ImageJ software (v. ImageJ2).

Migration (transwell) and invasion assay

For invasion assay, the Matrigel was diluted with serum-free medium in an appropriate proportion and added into a transwell chamber with a pore size of 8.0 μm. Then, they were placed in the incubator at 37°C for around 4 hours until the Matrigel solidified completely. For the migration assay, Matrigel does not need to be added. Then, the cells were suspended in FBS-free medium and spread to the upper chamber of the well, and the medium containing serum was added to the lower well. The migrated and invaded cells were fixed with 4% PFA and stained with 0.5% crystal violet, followed by measuring the number of migrated and invaded cells microscopically.

Cell proliferation assay

Taking measurement of the speed of cells was carried out according to the manufacturer of Cell Counting Kit 8 (CCK8; NCM Biotech). Briefly, 2000 cells were suspended in 100 μl and transferred into a 96-well plate. After cells adhered to the well, the medium was discarded, and the cells were washed with PBS. The fresh medium was again added, and 10 μl of CCK8 reagent was gently added into the corresponding well, followed by incubation at 37°C for 2 hours. Last, the absorbance of every well at 450 nm was measured by a Microplate Reader (Biotek) and recorded continuously for 5 days.

Statistics and reproducibility

All data involving statistics are presented as mean ± SEM. Statistical analysis was performed using GraphPad Prism software (version 8.0). The statistical significance was analyzed by Student's *t* test. $*P < 0.05$, $**P < 0.01$, $***P < 0.001$, and $****P < 0.0001$ indicate statistically substantial changes. For data presented without statistics, the experiment was repeated at least three times to ensure reproducibility, unless otherwise stated.

Supplementary Materials

The PDF file includes:

Figs. S1 to S14
Original blots S1 to S9
Legends for tables S1 to S6

Other Supplementary Material for this manuscript includes the following:

Tables S1 to S6

REFERENCES AND NOTES

1. P. Puchalska, P. A. Crawford, Multi-dimensional roles of ketone bodies in fuel metabolism, signaling, and therapeutics. *Cell Metab.* **25**, 262–284 (2017).
2. A. S. Williams, S. B. Crown, S. P. Lyons, T. R. Koves, R. J. Wilson, J. M. Johnson, D. H. Slentz, D. P. Kelly, P. A. Grimsrud, G. F. Zhang, D. M. Muoio, Ketone flux through BDH1 supports metabolic remodeling of skeletal and cardiac muscles in response to intermittent time-restricted feeding. *Cell Metab.* **36**, 422–437 (2024).
3. J. C. Newman, E. Verdin, β-Hydroxybutyrate: A signaling metabolite. *Annu. Rev. Nutr.* **37**, 51–76 (2017).
4. A. Pan, X. M. Sun, F. Q. Huang, J. F. Liu, Y. Y. Cai, X. Wu, R. N. Alolga, P. Li, B. L. Liu, Q. Liu, L. W. Qi, The mitochondrial β-oxidation enzyme HADHA restrains hepatic glucagon response by promoting β-hydroxybutyrate production. *Nat. Commun.* **13**, 386 (2022).
5. B. G. Allen, S. K. Bhatia, C. M. Anderson, J. M. Eichenberger-Gilmore, Z. A. Sibenaller, K. A. Mapuskar, J. D. Schoenfeld, J. M. Buatti, D. R. Spitz, M. A. Fath, Ketogenic diets as an adjuvant cancer therapy: History and potential mechanism. *Redox Biol.* **2**, 963–970 (2014).
6. O. Dmitrieva-Posocco, A. C. Wong, P. Lundgren, A. M. Golos, H. C. Descamps, L. Dohnalova, Z. Cramer, Y. Tian, B. Yueh, O. Eskiocak, G. Egervari, Y. Lan, J. Liu, J. Fan, J. Kim, B. Madhu, K. M. Schneider, S. Khoziainova, N. Andreeva, Q. Wang, N. Li, E. E. Furth, W. Bailis, J. R. Kelsen, K. E. Hamilton, K. H. Kaestner, S. L. Berger, J. A. Epstein, R. Jain, M. Li, S. Beyaz, C. J. Lengner, B. W. Katona, S. I. Grivennikov, C. A. Thaiss, M. Levy, β-hydroxybutyrate suppresses colorectal cancer. *Nature* **605**, 160–165 (2022).
7. G. Ferrere, M. Tidjani Alou, P. Liu, A. G. Goubet, M. Fidelle, O. Kepp, S. Durand, V. Iebba, A. Fluckiger, R. Daillere, C. Thelemaque, C. Grajeda-Iglesias, C. Alves Costa Silva, F. Aprahamian, D. Lefevre, L. Zhao, B. Ryffel, E. Colomba, M. Arnedos, D. Drubay, C. Rauber, D. Raoult, F. Asnicar, T. Spector, N. Segata, L. Derosa, G. Kroemer, L. Zitvogel, Ketogenic diet and ketone bodies enhance the anticancer effects of PD-1 blockade. *JCI Insight* **6**, e145207 (2021).
8. Y.-N. Qiao, L. Li, S.-H. Hu, Y.-X. Yang, Z.-Z. Ma, L. Huang, Y.-P. An, Y.-Y. Yuan, Y. Lin, W. Xu, Y. Li, P.-C. Lin, J. Cao, J.-Y. Zhao, S.-M. Zhao, Ketogenic diet-produced β-hydroxybutyric acid accumulates brain GABA and increases GABA/glutamate ratio to inhibit epilepsy. *Cell Discov.* **10**, 17 (2024).
9. Z. Xie, D. Zhang, D. Chung, Z. Tang, H. Huang, L. Dai, S. Qi, J. Li, G. Colak, Y. Chen, C. Xia, C. Peng, H. Ruan, M. Kirkey, D. Wang, L. M. Jensen, O. K. Kwon, S. Lee, S. D. Pletcher, M. Tan, D. B. Lombard, K. P. White, H. Zhao, J. Li, R. G. Roeder, X. Yang, Y. Zhao, Metabolic regulation of gene expression by histone lysine β-hydroxybutyrylation. *Mol. Cell* **62**, 194–206 (2016).

10. T. Zhou, X. Cheng, Y. He, Y. Xie, F. Xu, Y. Xu, W. Huang, Function and mechanism of histone β-hydroxybutyrylation in health and disease. *Front. Immunol.* **13**, 981285 (2022).
11. L. Sun, H. Zhang, P. Gao, Metabolic reprogramming and epigenetic modifications on the path to cancer. *Protein Cell* **13**, 877–919 (2022).
12. Y. F. Zheng, W. R. Sun, C. Shan, B. R. Li, J. Y. Liu, H. Xing, Q. L. Xu, B. P. Cui, W. J. Zhu, J. Chen, L. Y. Liu, T. Yang, N. Sun, X. B. Li, β-Hydroxybutyrate inhibits ferroptosis-mediated pancreatic damage in acute liver failure through the increase of H3K9bhb. *Cell Rep.* **41**, 111847 (2022).
13. S. Cornuti, S. W. Chen, L. Lupori, F. Finamore, F. Carli, M. Samad, S. Fenizia, M. Caldarelli, F. Damiani, F. Raimondi, R. Mazziotti, C. Magnan, S. Rocchiccioli, A. Gastaldelli, P. Baldi, P. Tognini, Brain histone beta-hydroxybutyrylation couples metabolism with gene expression. *Cell. Mol. Life Sci.* **80**, 28 (2023).
14. K. Tang, H. F. Zhang, J. H. Deng, D. H. Wang, S. C. Liu, S. Y. Lu, Q. F. Cui, C. Chen, J. C. Liu, Z. S. Yang, Y. G. Li, J. Chen, J. D. Lv, J. W. Ma, B. Huang, Ammonia detoxification promotes $CD8^+$ T cell memory development by urea and citrulline cycles. *Nat. Immunol.* **24**, 162–173 (2023).
15. W. G. Luo, Y. J. Yu, H. Wang, K. Liu, Y. Wang, M. L. Huang, C. H. Xuan, Y. N. Li, J. S. Qi, Up-regulation of MMP-2 by histone H3K9 β-hydroxybutyrylation to antagonize glomerulosclerosis in diabetic rat. *Acta Diabetol.* **57**, 1501–1509 (2020).
16. H. F. Zhang, K. Tang, J. W. Ma, L. Zhou, J. C. Liu, L. P. Zeng, L. Y. Zhu, P. W. Xu, J. Chen, K. K. Wei, X. Y. Liang, J. D. Lv, J. Xie, Y. Y. Liu, Y. H. Wan, B. Huang, Ketogenesis-generated β-hydroxybutyrate is an epigenetic regulator of $CD8^+$ T-cell memory development. *Nat. Cell Biol.* **22**, 18–25 (2020).
17. C. J. Terranova, K. M. Stemler, P. Barrodia, S. L. Jeter-Jones, Z. Q. Ge, M. D. Bonilla, A. Raman, C. W. Cheng, K. L. Allton, E. Arslan, Ö. H. Yilmaz, M. C. Barton, K. Rai, H. Piwnica-Worms, Reprogramming of H3K9bhb at regulatory elements is a key feature of fasting in the small intestine. *Cell Rep.* **37**, 110044 (2021).
18. H. Zhang, Z. Chang, L. N. Qin, B. Liang, J. X. Han, K. L. Qiao, C. Yang, Y. R. Liu, H. G. Zhou, T. Sun, MTA2 triggered R-loop trans-regulates BDH1-mediated β-hydroxybutyrylation and potentiates propagation of hepatocellular carcinoma stem cells. *Signal Transduct. Target. Ther.* **6**, 135 (2021).
19. J. H. Qin, X. H. Huang, S. S. Gou, S. T. Zhang, Y. J. Gou, Q. Zhang, H. Y. Chen, L. Sun, M. M. Chen, D. Liu, C. Han, M. Tang, Z. H. Feng, S. H. Niu, L. Zhao, Y. F. Tu, Z. X. Liu, W. M. Xuan, L. Z. Dai, D. Jia, Y. Xue, Ketogenic diet reshapes cancer metabolism through lysine β-hydroxybutyrylation. *Nat. Metab.* **6**, 7–23 (2024).
20. B. N. Sheikh, A. Akhtar, The many lives of KATs — Detectors, integrators and modulators of the cellular environment. *Nat. Rev. Genet.* **20**, 7–23 (2019).
21. S. Zhao, X. R. Zhang, H. T. Li, Beyond histone acetylation-writing and erasing histone acylations. *Curr. Opin. Struct. Biol.* **53**, 169–177 (2018).
22. Y. S. Xie, S. B. Du, Z. Y. Liu, M. Liu, Z. Q. Xu, X. J. Wang, J. X. Kee, F. Yi, H. Y. Sun, S. Q. Yao, Chemical biology tools for protein lysine acylation. *Angew. Chem. Int. Ed.* **61**, e202200303 (2022).
23. H. Huang, D. Zhang, Y. Weng, K. Delaney, Z. Tang, C. Yan, S. Qi, C. Peng, P. A. Cole, R. G. Roeder, Y. Zhao, The regulatory enzymes and protein substrates for the lysine β-hydroxybutyrylation pathway. *Sci. Adv.* **7**, eabe2771 (2021).
24. B. R. Sabari, D. Zhang, C. D. Allis, Y. M. Zhao, Metabolic regulation of gene expression through histone acylations. *Nat. Rev. Mol. Cell Biol.* **18**, 90–101 (2017).
25. Z. Kaczmarska, E. Ortega, A. Goudarzi, H. Huang, S. Kim, J. A. Márquez, Y. M. Zhao, S. Khochbin, D. Panne, Structure of p300 in complex with acyl-CoA variants. *Nat. Chem. Biol.* **13**, 21–29 (2017).
26. Y. H. Xiao, W. J. Li, H. Yang, L. L. Pan, L. W. Zhang, L. Lu, J. W. Chen, W. Wei, J. Ye, J. W. Li, G. H. Li, Y. Zhang, M. J. Tan, J. P. Ding, J. M. Wong, HBO1 is a versatile histone acyltransferase critical for promoter histone acylations. *Nucleic Acids Res.* **49**, 8037–8059 (2021).
27. J. Ohzeki, N. Shono, K. Otake, N. M. C. Martins, K. Kugou, H. Kimura, T. Nagase, V. Larionov, W. C. Earnshaw, H. Masumoto, KAT7/HBO1/MYST2 regulates CENP-A chromatin assembly by antagonizing Suv39h1-mediated centromere inactivation. *Dev. Cell* **37**, 413–427 (2016).
28. R. Yang, W. L. Peng, S. Shi, X. Peng, Q. D. Cai, Z. Y. Zhao, B. X. He, G. X. Tu, W. Yin, Y. C. Chen, Y. Q. Zhang, F. Liu, X. Wang, D. S. Xiao, Y. G. Tao, The NLRP11 protein bridges the histone lysine acetyltransferase KAT7 to acetylate vimentin in the early stage of lung adenocarcinoma. *Adv. Sci.* **10**, e2300971 (2023).
29. X. J. Li, W. L. Yu, X. Qian, Y. Xia, Y. H. Zheng, J. H. Lee, W. Li, J. X. Lyu, G. Rao, X. C. Zhang, C. N. Qian, S. G. Rozen, T. Jiang, Z. M. Lu, Nucleus-translocated ACSS2 promotes gene transcription for lysosomal biogenesis and autophagy. *Mol. Cell* **66**, 684–697 (2017).
30. P. Mews, G. Donahue, A. M. Drake, V. Luczak, T. Abel, S. L. Berger, Acetyl-CoA synthetase regulates histone acetylation and hippocampal memory. *Nature* **546**, 381–386 (2017).
31. P. Mews, G. Egervari, R. Nativio, S. Sidoli, G. Donahue, S. I. Lombroso, D. C. Alexander, S. L. Riesche, E. A. Heller, E. J. Nestler, B. A. Garcia, S. L. Berger, Alcohol metabolism contributes to brain histone acetylation. *Nature* **574**, 717–721 (2019).
32. D. Murthy, K. S. Attri, S. K. Shukla, R. Thakur, N. V. Chaika, C. He, D. Wang, K. Jha, A. Dasgupta, R. J. King, S. E. Mulder, J. Souchek, T. Gebregiworgis, V. Rai, R. Patel, T. Hu, S. Rana, S. S. Kollala, C. Pacheco, P. M. Grandgenett, F. Yu, V. Kumar, A. J. Lazenby, A. R. Black, S. Ulhannan, A. Jain, B. H. Edil, D. L. Klinkebiel, R. Powers, A. Natarajan, M. A. Hollingsworth, K. Mehla, Q. Ly, S. Chaudhary, R. F. Hwang, K. E. Wellen, P. K. Singh, Cancer-associated fibroblast-derived acetate promotes pancreatic cancer development by altering polyamine metabolism via the ACSS2–SP1–SAT1 axis. *Nat. Cell Biol.* **26**, 613–627 (2024).
33. R. Zhu, X. Ye, X. Lu, L. Xiao, M. Yuan, H. Zhao, D. Guo, Y. Meng, H. Han, S. Luo, Q. Wu, X. Jiang, J. Xu, Z. Tang, Y. J. Tao, Z. Lu, ACSS2 acts as a lactyl-CoA synthetase and couples KAT2A to function as a lactyltransferase for histone lactylation and tumor immune evasion. *Cell Metab.* **37**, 361–376.e7 (2025).
34. Z. T. Schug, B. Peck, D. T. Jones, Q. Zhang, S. Grosskurth, I. S. Alam, L. M. Goodwin, E. Smethurst, S. Mason, K. Blyth, L. McGarry, D. James, E. Shanks, G. Kalna, R. E. Saunders, M. Jiang, M. Howell, F. Lassailly, M. Z. Thin, B. Spencer-Dene, G. Stamp, N. J. van den Broek, G. Mackay, V. Bulusu, J. J. Kamphorst, S. Tardito, D. Strachan, A. L. Harris, E. O. Aboagye, S. E. Critchlow, M. J. Wakelam, A. Schulze, E. Gottlieb, Acetyl-CoA synthetase 2 promotes acetate utilization and maintains cancer cell growth under metabolic stress. *Cancer Cell* **27**, 57–71 (2015).
35. K. D. Miller, K. Pniewski, C. E. Perry, S. B. Papp, J. D. Shaffer, J. N. Velasco-Silva, J. C. Casciano, T. M. Aramburu, Y. V. V. Srikanth, J. Cassel, E. Skordalakes, A. V. Kossenkov, J. M. Salvino, Z. T. Schug, Targeting ACSS2 with a transition-state mimetic inhibits triple-negative breast cancer growth. *Cancer Res.* **81**, 1252–1264 (2021).
36. S. A. Comerford, Z. Huang, X. Du, Y. Wang, L. Cai, A. K. Witkiewicz, H. Walters, M. N. Tantawy, A. Fu, H. C. Manning, J. D. Horton, R. E. Hammer, S. L. McKnight, B. P. Tu, Acetate dependence of tumors. *Cell* **159**, 1591–1602 (2014).
37. Q. Li, H. Luo, F.-Q. Dai, R.-T. Wang, X.-Q. Fan, Y.-Y. Luo, M.-S. Deng, Y. Wang, T. Long, W. Guo, B. Xu, C.-X. Xu, H. Jin, SAMD9 promotes postoperative recurrence of esophageal squamous cell carcinoma by stimulating MYH9-mediated GSK3β/β-catenin signaling. *Adv. Sci.* **10**, e2203573 (2023).
38. W. Shao, J. Li, Q. Piao, X. Yao, M. Li, S. Wang, Z. Song, Y. Sun, L. Zheng, G. Wang, L. Liu, C. Yu, Y. Huang, Y. Bao, L. Sun, FRMD3 inhibits the growth and metastasis of breast cancer through the ubiquitination-mediated degradation of vimentin and subsequent impairment of focal adhesion. *Cell Death Dis.* **14**, 13 (2023).
39. K. L. Diehl, T. W. Muir, Chromatin as a key consumer in the metabolite economy. *Nat. Chem. Biol.* **16**, 620–629 (2020).
40. S. Trefely, K. Huber, J. Liu, M. Noji, S. Stransky, J. Singh, M. T. Doan, C. D. Lovell, E. von Krusenstiern, H. Jiang, A. Bostwick, H. L. Pepper, L. Izzo, S. Zhao, J. P. Xu, K. C. Bedi Jr., J. E. Rame, J. G. Bogner-Strauss, C. Mesaros, S. Sidoli, K. E. Wellen, N. W. Snyder, Quantitative subcellular acyl-CoA analysis reveals distinct nuclear metabolism and isoleucine-dependent histone propionylation. *Mol. Cell* **82**, 447–462.e6 (2022).
41. M. Russo, F. Gualdrini, V. Vallelonga, E. Prosperini, R. Noberini, S. Pedretti, C. Borriero, P. Di Chiaro, S. Polletti, G. Imperato, M. Marenda, C. Ghirardi, F. Bedin, A. Cuomo, S. Rodighiero, T. Bonaldi, N. Mitro, S. Ghisletti, G. Natoli, Acetyl-CoA production by mediator-bound 2-ketoacid dehydrogenases boosts de novo histone acetylation and is regulated by nitric oxide. *Mol. Cell* **84**, 967–980.e10 (2024).
42. W. Chen, X. Yu, Y. Wu, J. Tang, Q. Yu, X. Lv, Z. Zha, B. Hu, X. Li, J. Chen, L. Ma, J. L. Workman, S. Li, The SESAME complex regulates cell senescence through the generation of acetyl-CoA. *Nat. Metab.* **3**, 983–1000 (2021).
43. Y. Wang, Y. R. Guo, K. Liu, Z. Yin, R. Liu, Y. Xia, L. Tan, P. Yang, J.-H. Lee, X.-j. Li, D. Hawke, Y. Zheng, X. Qian, J. Lyu, J. He, D. Xing, Y. J. Tao, Z. Lu, KAT2A coupled with the α-KGDH complex acts as a histone H3 succinyltransferase. *Nature* **552**, 273–277 (2017).
44. K. J. Menzies, H. Zhang, E. Katsyuba, J. Auwerx, Protein acetylation in metabolism — Metabolites and cofactors. *Nat. Rev. Endocrinol.* **12**, 43–60 (2016).
45. V. Gouirand, T. Gicquel, E. C. Lien, E. Jaune-Pons, Q. Da Costa, P. Finetti, E. Metay, C. Duluc, J. R. Mayers, S. Audebert, L. Camoin, L. Borge, M. Rubis, J. Leca, J. Nigri, F. Bertucci, N. Dusetti, J. L. Iovanna, R. Tomasini, G. Bidaut, F. Guillaumond, M. G. Vander Heiden, S. Vasseur, Ketogenic HMG-CoA lyase and its product β-hydroxybutyrate promote pancreatic cancer progression. *EMBO J.* **41**, e110466 (2022).
46. Z. Niu, C. Chen, S. Wang, C. Lu, Z. Wu, A. Wang, J. Mo, J. Zhang, Y. Han, Y. Yuan, Y. Zhang, Y. Zang, C. He, X. Bai, S. Tian, G. Zhai, X. Wu, K. Zhang, HBO1 catalyzes lysine lactylation and mediates histone H3K9la to regulate gene transcription. *Nat. Commun.* **15**, 3561 (2024).
47. J. Shang, S. Wang, A. Wang, F. Li, J. Zhang, J. Wang, R. Lv, H. Chen, X. Mu, K. Zhang, X. Bai, Y. Tian, Intra-ovarian inflammatory states and their associations with embryo quality in normal-BMI PCOS patients undergoing IVF treatment. *Reprod. Biol. Endocrinol.* **22**, 11 (2024).
48. H. Dong, J. Zhang, H. Zhang, Y. Han, C. Lu, C. Chen, X. Tan, S. Wang, X. Bai, G. Zhai, S. Tian, T. Zhang, Z. Cheng, E. Li, L. Xu, K. Zhang, YiaC and CobB regulate lysine lactylation in *Escherichia coli*. *Nat. Commun.* **13**, 6628 (2022).
49. T. J. Erb, I. A. Berg, V. Brecht, M. Müller, G. Fuchs, B. E. Alber, Synthesis of C5-dicarboxylic acids from C2-units involving crotonyl-CoA carboxylase/reductase: The ethylmalonyl-CoA pathway. *Proc. Natl. Acad. Sci. U.S.A.* **104**, 10631–10636 (2007).

50. L. Yin, L. Xiao, Y. Gao, G. Wang, H. Gao, Y. Peng, X. Zhu, J. Wei, Y. Miao, K. Jiang, Z. Lu, Comparative bioinformatical analysis of pancreatic head cancer and pancreatic body/tail cancer. *Med. Oncol.* **37**, 46 (2020).
51. J. Iqbal, Z.-N. Tan, M.-X. Li, H.-B. Chen, B. Ma, X. Zhou, X.-M. Ma, Estradiol alters hippocampal gene expression during the estrous cycle. *Endocr. Res.* **45**, 84–101 (2019).

Acknowledgments
Funding: This work was financially supported by the National Natural Science Foundation of China [22274114 (K.Z.), 22474090 (K.Z.), and 22374106 (G.Z.)] and the Talent Excellence Program from Tianjin Medical University. **Author contributions:** K.Z. administrated and supervised the project. G.Z. and K.Z. acquired the funding for supporting the project. K.Z. and S.W. provided the resources for the project. S.W., Z.N., R.Z., G.Z., and K.Z. designed the experiments (methodology or conceptualization). S.W., Z.N., Y.Zhan., R.Z., Y.S., J.Z., Y.Za., and G.Z. conducted the experiments (investigation). S.W., Z.N., Y.H., and H.Z. acquired the data (investigation). S.W., Z.N., and A.W. analyzed the data (formal analysis). S.W. and Z.N. visualized the data. S.W., Z.N., and R.Z. validated the data, and S.W., Z.N., and K.Z. performed the data curation. G.Z. and S.W. wrote the manuscript. G.Z., R.L., Y. Zhao, and K.Z. revised the manuscript. K.Z. approved the final manuscript. **Competing interests:** The authors declare that they have no competing interests. **Data and materials availability:** All data needed to evaluate the conclusions in the paper are present in the paper and/or the Supplementary Materials. The MS proteomics data have been deposited to the ProteomeXchange Consortium via the PRIDE partner repository with the dataset identifiers PXD051685, PXD051668, and PXD051692. Raw data of CUT&Tag and RNA-seq can be obtained at the Gene Expression Omnibus database under accession nos. GSE267130 (CUT&Tag) and GSE267129 (RNA-seq).

Submitted 9 January 2025
Accepted 11 July 2025
Published 15 August 2025
10.1126/sciadv.adv8448